Hot Corrosion of Inconel 625 Overlay Weld Cladding in Smelting Off-Gas Environment

E. MOHAMMADI ZAHRANI and A.M. ALFANTAZI

Degradation mechanisms and hot corrosion behavior of weld overlay alloy 625 were studied. Phase structure, morphology, thermal behavior, and chemical composition of deposited salt mixture on the weld overlay were characterized utilizing XRD, SEM/EDX, DTA, and ICP/OES, respectively. Dilution level of Fe in the weldment, dendritic structure, and degradation mechanisms of the weld were investigated. A molten phase formed on the weld layer at the operating temperature range of the boiler, which led to the hot corrosion attack in the water wall and the ultimate failure. Open circuit potential and weight-loss measurements and potentiodynamic polarization were carried out to study the hot corrosion behavior of the weld in the simulated molten salt medium at 873 K, 973 K, and 1073 K (600 °C, 700 °C, and 800 °C). Internal oxidation and sulfidation plus pitting corrosion were identified as the main hot corrosion mechanisms in the weld and boiler tubes. The presence of a significant amount of Fe made the dendritic structure of the weld susceptible to preferential corrosion. Preferentially corroded (Mo, Nb)-depleted dendrite cores acted as potential sites for crack initiation from the surface layer. The penetration of the molten phase into the cracks accelerated the cracks' propagation mainly through the dendrite cores and further crack branching/widening.

I. INTRODUCTION

KIVCET lead and zinc smelters are used in service as a modern, direct smelting process.[1,2] A schematic of the KIVCET furnace and its 30-m-tall radiant boiler, as well as a section of the water wall tubes, can be seen in Figure 1. High pressure water flows inside the tubes to extract heat from the high temperature off-gas of the smelter. The off-gas is in contact with the fireside (hot side) of the tubes. The large radiant shaft boiler and a subsequent convection boiler to cool the off-gas of the smelter are two parts of the smelter. Based on Figure 1, the off-gas from the reaction shaft at 1648 K (1375 °C) enters the 717 m^2 vertical radiant boiler of the membrane wall construction by means of an uptake shaft, constructed with water-cooled copper elements. In the radiant section of the boiler, the off-gas is cooled to 1073 K (800 °C) prior to entering the down-coming section of the boiler. The total surface area of the down-coming section of the boiler is about 486 m^2 and the temperature of the off-gas decreased to 873 K (600 °C) in this section. Afterward, the off-gas enters the convection section of the boiler with a total area of 1012 m^2 and reduces the final gas temperature to 598 K (325 °C). The final stages of cooling occurred in an adiabatic sprayed tower and cooling tower, where the temperature of the gas lowered to 338 K and 291 K (65 °C and 18 °C), respectively.[3]

In the radiant section of the boiler, the original boiler tubes were constructed of carbon steel. These tubes were experiencing unacceptably high corrosion rates because of the severely aggressive working conditions in the boiler environment. Consequently, significant wall thinning occurred in the tubes. Strength and structure integrity of carbon steel tubes, resistance of the tubes to high temperature and high pressure water and steam (used in heat transfer), and relatively low cost of the carbon steel are the key benefits of using the carbon steel in manufacturing water wall tubes of different types of boilers.[4] However, carbon steel does not have satisfactory resistance to corrosion at elevated temperatures.

An alloy 625 (UNS N06625) was applied as a weld overlay on the water wall tubes of the radiant boiler by an automatic gas metal arc welding (GMAW) process to control/reduce the corrosion rate of the tubes. This process was done on-site in the boiler. In order to achieve a uniform coverage of the water wall (i.e., membranes and tubes), the weld beads were deposited by the GMAW technique in a vertical down mode starting from the membrane and then moving to the tube section based on a pre-programed weld bead sequence. Multiple welding passes were performed to fully cover the surface of the water wall with a single layer of the weld deposit. The wire transfer mode was either sprayed or pulsed sprayed during welding. A single-layer GMAW overlay was followed by a gas tungsten arc welding (GTAW) wash pass. The GTAW wash pass remelted the GMAW deposit without any filler addition. The technical details of the GMAW

E. MOHAMMADI ZAHRANI, Ph.D. Candidate, and A.M. ALFANTAZI, Professor and Associate Dean of Research and Graduate Studies, Faculty of Applied Science at UBC, are with the Corrosion Research Group, Department of Materials Engineering, The University of British Columbia (UBC), 309-6350 Stores Road, Vancouver, BC V6T1Z4, Canada. Contact e-mail: ehsanmoh@mail.ubc.ca
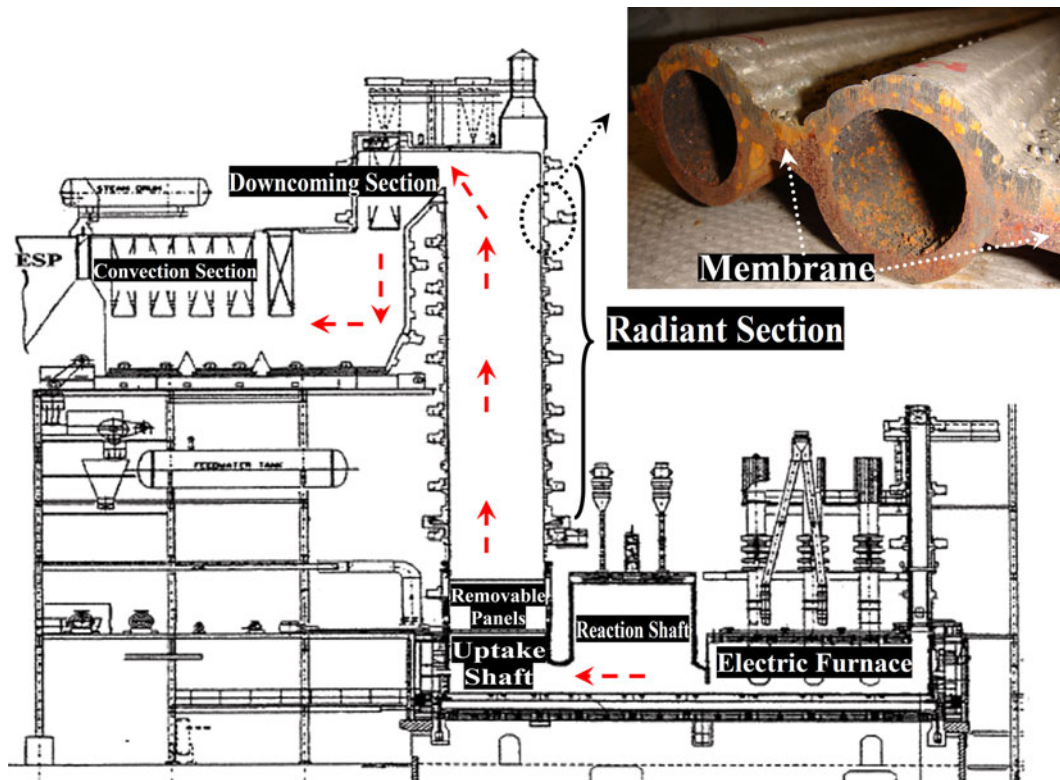
Fig. 1—A schematic of the KIVCET waste heat boiler and an image of the water wall tubes in the radiant section of the boiler.

technique were as follows: type of polarity: DC reverse (DCEP); amperage range: 190 to 225 A; voltage range: 21 to 27.5 V; minimum travel speed: 0.01 m/s (25 inches per minute, IPM); and maximum heat input rate: 593,622 J/m (15,078 Joule per inch, J/In). GTAW parameters were selected as follows: type of polarity: DC straight (DCEN, non-pulsed); amperage range: 350 to 435 A; voltage range: 12 to 16.5 V; minimum travel speed: 0.01 m/s (25 IPM); and maximum heat input rate: 687,559 J/m (17,464 J/In). In both GMAW and GTAW techniques, amperage, voltage, and travel speed were carefully controlled in the mentioned ranges to assure that the maximum heat input did not exceed the specified maximum heat input rates at any time during welding. Heat input was calculated by multiplying welding voltage × welding amperage × 60 and dividing the results by travel speed (IPM). The resultant value was heat input, measured in J/In. According to the presented images of the water wall in Figures 1 and 2, each of the weld beads was overlapped by the subsequent weld bead to ensure full coverage with no missing spots. The average thickness of the weld overlay was about 3.38 ± 0.5 mm, determined by cross-sectional SEM analysis of the overlaid tubes in this study. The application of alloy 625 weld overlay or cladding applied by the GMAW process is known as the current prevailing cost-effective and long-term protection method for providing life extension for boilers in a diverse range of corrosive environments.[4] Reportedly, the weld overlaying technique can provide a dense coating layer which is chemically bonded to the base metal with a thickness of several millimeters.[5] It is worth mentioning that weld cladding has been widely used in waste-to-energy (WTE) boilers in the waste incinerator industry to protect boiler tubes against the harsh corrosive working environment of the boiler although it is very costly, ~€2,000 to €2,500 per square meter.[6] A wide range of reports on the successful application of weld overlay alloy 625 in the waste incinerator industry and WTE boilers to mitigate the corrosion issue was the main reason to select this strategy for protecting the water wall tubes of the radiant boiler in the KIVCET smelter against corrosion attack. However, in the radiant shaft boiler, the corrosion rate of the alloy 625 weld overlay and the boiler tubes is still unacceptably high, which led to ultimate failure of the weld overlay.

Deposition of salt mixtures on the water wall tubes occurred in the radiant boiler environment. The presence of these deposits seems to be an important factor in exacerbating the corrosivity of the boiler environment and accelerating the degradation of the weld overlay and tubes. A mechanical hammer was periodically used in the radiant boiler to hit the water walls, which caused the physical removal of the deposited salt on the water walls, to facilitate the heat transfer through the tubes. A sample of the failed overlaid tubes from the KIVCET waste heat boiler, received for evaluation and failure analysis study, can be seen in Figure 2.

Prior to the use of the GMAW technique for applying the weld overlay alloy 625 in this boiler, the plasma spray (APS) technique had been utilized to perform an alloy 625 coating on the water wall tubes of the boiler
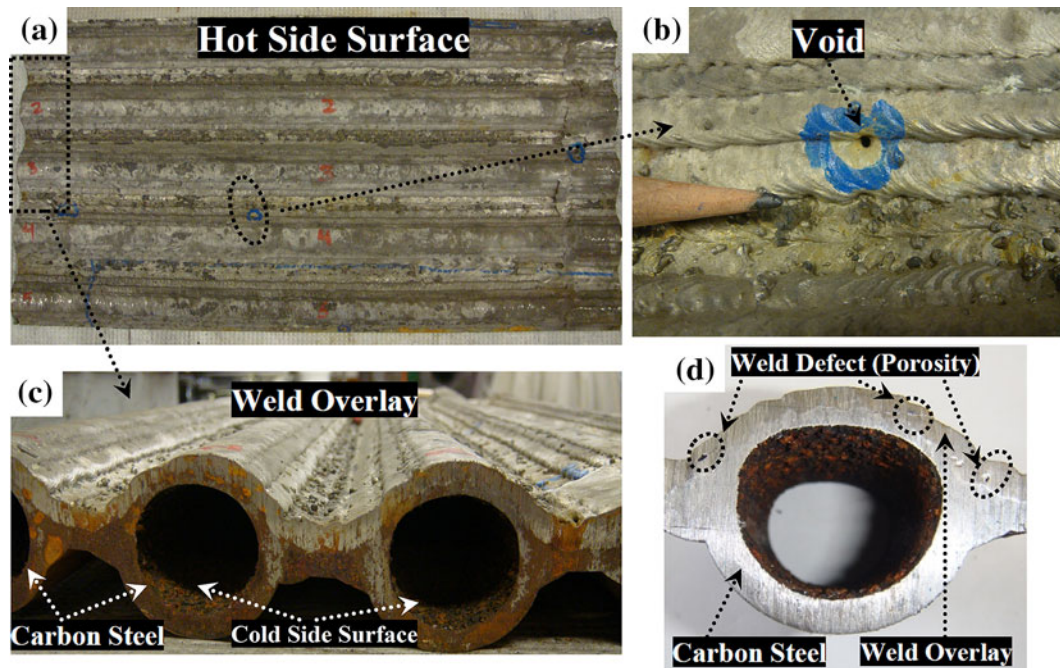
Fig. 2—(*a*) and (*c*) A sample of the failed water wall, coated by the weld overlay alloy 625; (*b*) a well-developed cavity formed in the weld overlay in the boundary of two weld beads; and (*d*) a cross section of the failed tube after grounding, showing the presence of porosities in the weld overlay.

for protection purposes. However, the plasma-sprayed coating was not able to act as an effective barrier layer to protect the tubes against the corrosive environment and its long-term performance was not acceptable. The porous nature of the plasma-spayed coating facilitated the penetration of the deposited salt mixtures through the coating to the tubes. Because of the weak bond strength of the plasma-sprayed coating and its relatively thin thickness, the plasma-sprayed alloy 625 coating did not demonstrate an appropriate durability in this application. Consequently, ultimate failure of the plasma-sprayed alloy 625 coating happened after several months of being in service. This can justify the selection of the GMAW technique for performing weld overlay alloy 625 on the water wall tubes of the radiant boiler in the KIVCET smelter to provide protection against corrosion. A coating is protective if it prevents outward diffusion of metal cations and inward diffusion of elements that can react with substrate material.[7] However, interconnected porosities, oxide-containing splat boundaries, and compositional inhomogeneities, which can be created through a plasma-spraying process, significantly limit the corrosion resistance of the plasma-sprayed coatings.[7]

Alloy 625 is a high-chromium, high-molybdenum, nickel-based superalloy, which has been widely used in the form of weld overlay and plasma-sprayed coatings for high temperature protection applications in many corrosive environments such as gas turbines, waste-fired boilers, as well as in pulp and paper industries.[5,8] Preventing high temperature oxidation and hot corrosion at elevated temperatures due to oxidation resistance of alloy 625 is the main purpose for this broad range of applications.[8]

Alloys used in some environments, such as power generation machines, gas turbines, WTE boilers, industrial waste incinerators, pulp and paper industries, coal-fired boilers, oil-fired boilers, furnaces, and black liquor recovery boilers, sometimes undergo an aggressive mode of corrosion attack associated with the formation of salt deposits on their surfaces at elevated temperatures. This deposit-induced accelerated corrosion is called "hot corrosion."[9,10] Hot corrosion is the most prevalent mode of attack and failure at high temperature, particularly where the surface of the alloy is covered by deposited salt mixtures. Reportedly, 5 to 10 pct of operating costs in the above-mentioned plants are attributed to the high temperature corrosion/hot corrosion failure and related maintenance costs.[1,11,12]

Despite the wide range of weld overlay Inconel 625 applications to protect water wall tubes in different types of boilers and to reduce corrosion rates of boiler tubes in energy production applications, there is no systematic study on investigating hot corrosion resistance and failure of the weld overlay alloy 625 at high temperatures in the presence of deposited salt mixtures. In particular, the corrosive environment of the radiant boiler in the KIVCET flash lead smelter is unique due to the presence of deposited salts containing heavy metals such as lead, zinc, and cadmium, together with chlorine, oxygen, and sulfur. The hot corrosion failure mechanism of the weld overlay alloy 625 in this environment when deposited salts exist, as well as characteristics of the deposited salts, is not well understood yet. Because of the strict economic considerations in these kinds of plants, costs related to the maintenance of the plant, including failure costs and related downtime

and periodic shutdowns, must be reduced as much as possible.[1] From this perspective, conducting a detailed investigation to determine the root cause of the failure in the overlaid tubes and hot corrosion behavior of the alloy 625 weld overlay is of important economic value as well as scientific and technical interest.

II. EXPERIMENTAL PROCEDURE

A. Deposited Salts Mixture Characterization

Salt mixtures deposited on the water wall tubes of the radiant boiler were characterized to determine chemical composition, phase analysis, morphology, and thermal behavior of the actual deposits. The deposits were gathered from the surfaces of the water wall tubes during one of the periodical shutdowns of the plant. The morphology and physical condition of the deposits can be seen in Figure 3. Based on the physical condition and morphology, the deposited mixture in Figure 3(a) was split into four groups of samples (Samples 1 to 4) and each sample was separately characterized. Samples 1 to 4 can be seen in Figures 3(b), (c), (d), and (e), respectively.

Phase analysis of the deposits was studied by the X-ray diffraction technique (XRD: Rigaku MultiFlex, Tokyo, Japan) and using Ni-filtered Cu Kα ($\lambda_{Cu\ K\alpha}$ = 0.154186 nm, radiation at 40 kV and 20 mA) over the 2θ range of 10 to 80 deg (scan speed: 2 degrees per minute; and step size: 0.04 degrees). Obtained XRD patterns were compared to the standards compiled by the Joint Committee on Powder Diffraction and Standards (JCPDS) to identify phases. Chemical composition of the deposits was determined by inductively coupled plasma/atomic absorption spectroscopy (ICP/AAS: Inspectorate-International Plasma Laboratory, IPL, BC, Canada). Microstructure and morphology of the deposited salts were also characterized by scanning electron microscopy with light-metal, energy-dispersive X-ray spectroscopy (SEM/EDX: Hitachi S-3000N, Tokyo, Japan). For this purpose, the deposited salts were mounted in a cold epoxy resin. The mounted samples were ground on 600, 1200, and 2400-grit silicon carbide papers followed by polishing on 6, 1, and 0.5 μm polishing pads. The deposits were examined by differential thermal analysis (DTA: Linseis L70/2171, Linseis Inc., Selb, Germany) in air atmosphere from ambient temperature up to 1473 K (1200 °C) at a heating rate of
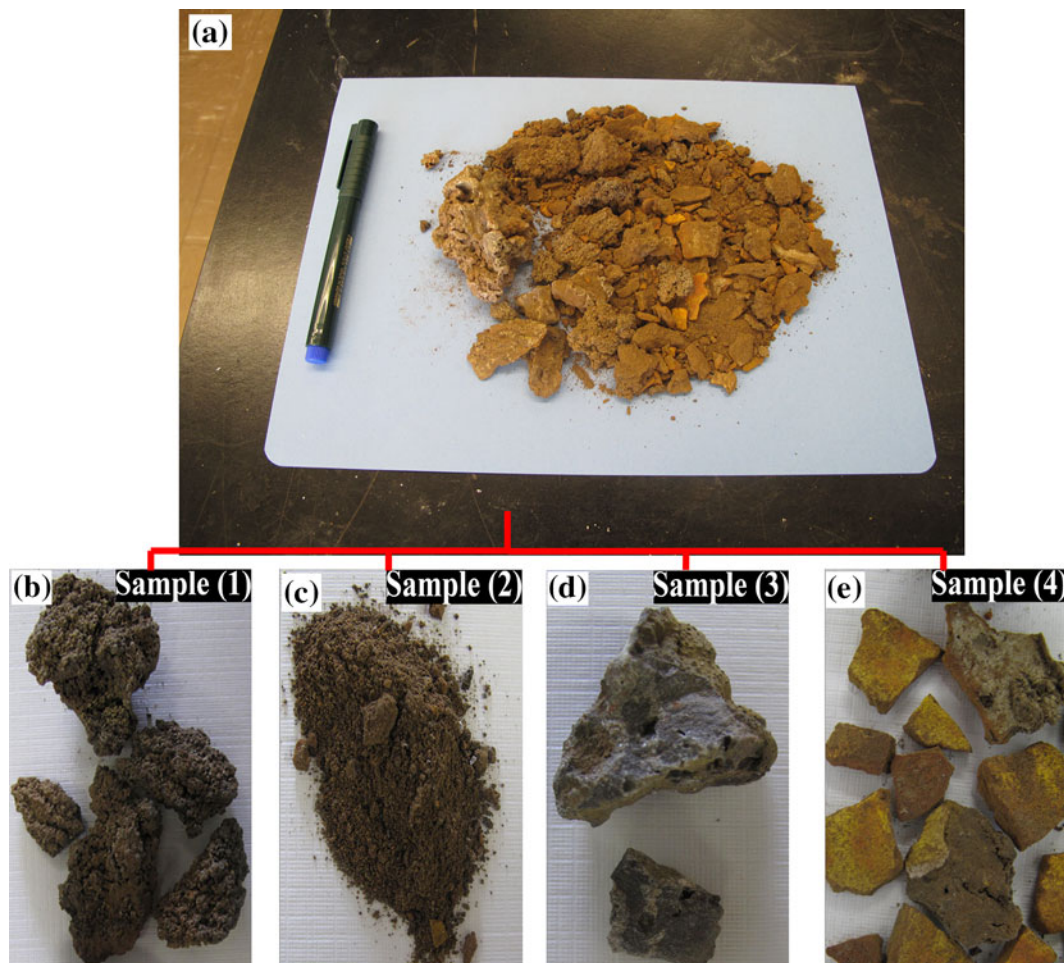

Fig. 3—(a) Morphology and physical condition of the actual deposited salt mixtures on the water wall of the boiler; [(b) to (e)] show different groups of the samples, selected from the actual salt mixture in (a) for characterization purposes.

10 K min^{-1} (10 °C min^{-1}) to evaluate thermal behavior of the mixtures and to determine liquidus temperatures. Characterization of the deposits was important for designing a simulated salt mixture used as an electrolyte in electrochemical tests to study hot corrosion resistance of the weld overlay.

B. Metallographic Study

A part of the failed water wall was cut to investigate the condition of the weldment and the substrate. This part was partially covered by the deposited salt mixtures during service in the boiler. It was perfectly cleaned from the deposited salts and corrosion products. The methodology for characterization of the deposited salts is explained in Section II–A. This part of the failed water wall was a window portion, containing five tubes. This perfectly cleaned sample can be seen in Figure 2. The sample had two sides, including the front side covered with the weld overlay alloy 625 and facing the hot off-gas of the smelter (hot side surface, HSS), and the back side (cold side surface, CSS). HSS is the surface exposed to the deposited salts during service in the radiant boiler environment. After visual inspection, dye penetrant and fluorescent dye penetrant tests were conducted on the HSS in this part of the failed water wall. Afterward, several groups of samples were cut from different locations in this part of the failed water wall for metallographic examination. Locations of the samples were selected based on the results of visual examinations, fluorescent dye penetrant tests, and the conducted SEM studies on the surface of the weld overlay. For a cross-sectional metallographic study, the mounted samples were ground with silicon carbide (grit range of 80 to 4000) and subsequently diamond polished down to 6, 1, and finally 0.05 μm. The polished samples were studied by an optical microscope and SEM/EDX. Preparation of the specimens for the metallographic study was done based on the ASTM E3-11.[13] ISO/DIS 26146 standard was also considered for the metallographic examination of the samples.[14] To observe the microstructure of the alloy 625 weld overlay on the failed tubes, polished samples of the weld overlay were etched in a solution containing 5 mL H$_2$SO$_4$, 3 mL HNO$_3$, and 92 mL HCl.[15]

C. High Temperature Electrochemical Study and Weight-Loss Measurement

Open circuit potential measurement (OCP), potentiodynamic polarization, and weight-loss measurement techniques were utilized to study hot corrosion susceptibility of the alloy 625 weld overlay. A three-electrode electrochemical cell arrangement was prepared for conducting the electrochemical tests. The electrochemical cell was constituted by the working electrode (WE) (weld overlay alloy 625) and two 1.2-mm-diameter/500-mm-long platinum wires as auxiliary and pseudo-reference electrodes, which were immersed directly in the molten salt medium. Platinum wires were woven together to produce a mesh-like counter electrode (CE). The mesh-like CE to the WE surface ratio was equal to 5 (CE:WE = 5:1). All platinum electrodes were cleaned and abraded using 600-grit SiC sand paper, ultrasonically washed in ethanol and then in acetone, and dried under a warm air stream before being isolated in alumina tubes and sealed with refractory cement, leaving 25-mm-long free length to make direct contact with the corrosive molten salt. The weld overlay alloy 625 WEs had a rectangular shape with dimensions of 20 × 10 × 2 mm. The details of the procedure which was followed to select the pure platinum as the pseudo-reference electrode were discussed elsewhere.[1] Our previous study confirmed that pure platinum is a suitable choice to be used as a reference and CE.[1]

On a laboratory scale, it was not technically possible to produce an alloy 625 weld overlay with characteristics exactly similar to the weld overlay alloy 625 in the radiant boiler. For this reason, weld overlay samples were carefully cut from specific locations of the water wall in the radiant boiler, which were in sound condition. In these locations, no macroscopic or microscopic signs of corrosion attack were observed in the weld overlay. These samples of weld overlay alloy 625 were used to prepare the WEs for conducting the hot corrosion electrochemical studies. The microstructure of the weld overlay alloy 625 WE prior to the test can be seen in Figure 4. The chemical composition of the weld overlay alloy 625 was determined by ICP/AAS analysis (Table I).

For preparation of the WEs, rectangular pieces of the weld overlay alloy 625 were ground to 600-grit silicon carbide paper, rinsed with distilled water, ultrasonically degreased with acetone, and dried under a warm air stream. A wire made of 80Cr-20Ni (wt pct) was spot welded to each sample to provide an electrical connection between the WE and potentiostat. The alumina tubes were used to isolate the 80Cr-20Ni wire and the gap between the ceramic tube and the wire was filled with the refractory cement (Ceramabond: Aremco Products Inc., NY, USA). All alumina tubes, which were used for preparation of the pseudo-reference, counter, and WEs, were replaced after each test. A simulated molten salt medium was used as an electrolyte. Analytical-grade PbSO$_4$ and CdO (Sigma-Aldrich, MO, USA), Pb$_3$O$_4$ (Alfa Aesar, MA, USA), PbCl$_2$ (Anachemia, QC, Canada), and ZnO (Fisher Scientific, NH, USA) were used to prepare the simulated salt mixture. For preparation of the simulated salt mixture, measured amounts of the necessary chemical compounds (Table II) were milled to ensure homogeneity. The elemental analysis of the prepared salt mixture is presented in Table III. The composition of the simulated salt mixture was selected based on the chemical composition of the deposited corrosive salt mixtures on the water wall tubes.[1,10,16] Specific amounts of the prepared simulated salt mixture (15 g cm^{-2} of the initial area of the specimen) were introduced into a 30-mL alumina crucible, to give a melt depth of about 3.5 cm. The crucible was then set inside a vertical electrical furnace to reach the test temperature, which was measured constantly during the tests using a type K thermocouple under dynamic air atmosphere (flow rate: 200 mL min^{-1}). The crucible together with the solid corrosive salt mixture was replaced for each
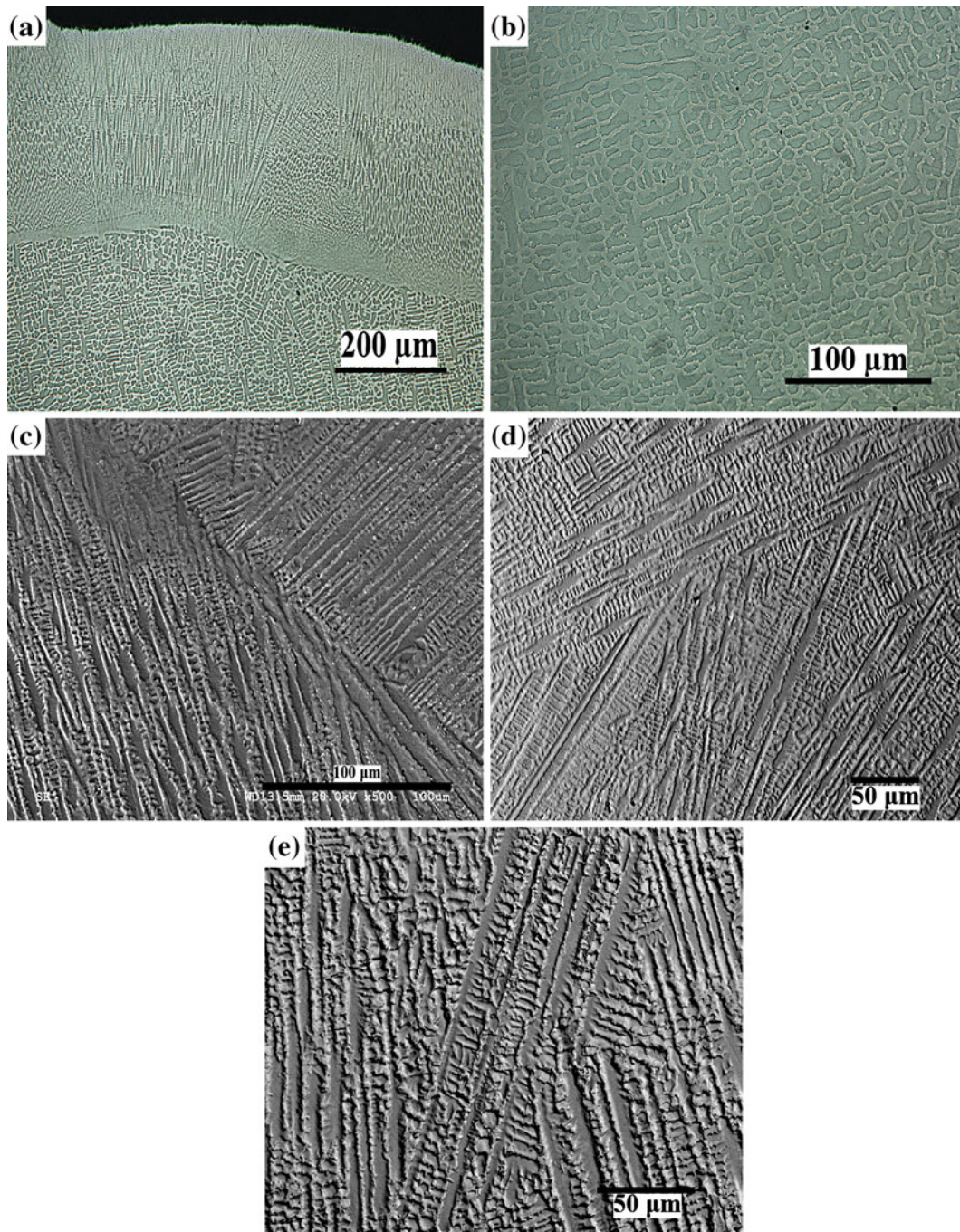
Fig. 4—Optical (*a*, *b*) and SEM [(*c*) to (*e*)] photomicrographs of the weld overlay alloy 625, showing the microstructure and the dendritic solidification in the weld overlay.

Table I. Chemical Composition (Weight Percent) of Weld Overlay Alloy 625, Carbon Steel Tube (Substrate), and Alloy 625 Consumable Electrode (Filler Metal)

	Ni	Cr	Mo	Fe	Nb	Ti	Co	Zn	Al	C	S	Si	Mn	Zr
Weld Overlay	bal.	17.02	6.00	23.64	2.85	0.25	<0.0001	0.25	0.35	0.05	0.01	0.30	0.17	1.9
Base Metal	0.01	0.06	0.01	bal.	—	<0.01	0.0013	0.001	0.03	0.16	0.02	0.39	0.39	0.08
Filler Metal	64.50	22.19	8.67	0.383	3.61	0.201	0.044	—	0.095	0.008	0.001	0.072	0.042	—

**Table II. Chemical Composition (Weight Percent)
of Prepared Simulated Salt Mixture**

	$PbSO_4$	$PbCl_2$	Pb_3O_4	ZnO	CdO
Salt Mixture	47	7	13	23	5

**Table III. Elemental Analysis (Weight Percent) of Prepared
Simulated Salt Mixture**

	Pb	Cl	S	Zn	Cd
Salt Mixture	48.1	1.7	5.0	18.6	4.4

experiment. The potentiostat used in the electrochemical experiments was a Princeton Applied Research (PAR) model 273A with M352 analysis software. Once the crucible containing the simulated salt mixture was set into the electrical tube furnace, the electrochemical cell was introduced inside the crucible and corresponding wires of the potentiostat were connected to the electrochemical cell. Electrochemical tests were carried out at 873 K, 973 K, and 1073 K (600 °C, 700 °C, and 800 °C). The OCP of the cell was recorded during the first 24 hours of immersion in the molten salt electrolyte. Before performing the potentiodynamic polarization test, the OCP of the cell must reach a stable value and the system must be at an equilibrium condition. A WE's potential was continuously increased from −200 to +1200 mV with respect to the OCP at a scan rate of 0.166 mV/s during the potentiodynamic polarization tests. Selection of the potentiodynamic potential sweep rate of 0.6 V/h (0.166 mV/s) for performing the polarization tests was based on the requirements of ASTM G59-97[17] and ASTM G5-94.[18] In order to determine the corrosion rate of the weld overlay, the weight-loss measurement technique was used. Utilizing this simple technique for corrosion rate determination has been recommended to reduce the probability of introducing systematic errors into the obtained results.[1] The followed standard methodology for conducting the weight-loss measurement study was accurately described elsewhere.[1] The standard weight-loss measurement (gravimetric) method, also known as the embedded test, was carried out under the same experimental conditions as that for the electrochemical tests.

In order to determine the type and mechanism of the corrosion attack, scales and corrosion products must be removed from the corroded surfaces. For this purpose, the corroded sample was physically cleaned under the compressed air stream and washed in boiling, distilled water for 30 minutes, followed by ultrasonic cleaning in a bath of alcohol for 1 hour to remove the loose and bulky corrosion products and deposits. Then, the standard methodology presented in ASTM G1-03[19] was followed to chemically remove the rest of the scales. This standard methodology was carefully followed to ensure that the corroded sample was perfectly cleaned from the corrosion products and scales. This must be done to observe the surface directly exposed to the molten salt medium through the SEM, determining the type and mechanism of the corrosion attack. For

cross-sectional SEM analysis, the cross section of the corroded sample was mounted in a cold epoxy resin. The mounted sample was ground on 600, 1200, and 2400-grit silicon carbide papers, followed by polishing on 6, 1, and 0.5 μm polishing pads. The amounts of the dissolved alloying elements in the molten salt electrolyte were quantitatively measured using ICP/AAS analysis.

III. RESULTS AND DISCUSSION

A. Deposited Salt Mixture

Due to the importance of the salt mixtures deposited on the water wall tubes on degradation and failure of the weld overlay alloy 625, having detailed information about phase structure and chemistry of the deposits is essential to developing a better understanding of the root cause of the failure/degradation in the weld overlay and the role of the deposited salts in this phenomenon.[16] With regards to the deposited salt mixture characterization, some results were described in our previous report[16] and further details and discussions have been mentioned in the current report for completeness. Figure 5 presents XRD patterns of samples 1 to 4, which are deposited on the failed water wall tubes. The general appearance of samples 1 to 4 of the deposited salt mixtures can be seen in Figure 3. Based on the XRD results, $PbSO_4$ (anglesite), $PbO_{1.55}$, PbS (galena), and $Pb_2(SO_4)O$ (lanarkite) [$Pb(SO_4)$ + PbO] phases were the main Pb-containing phases in the structure of samples 1 to 3. The strongest intensity of the diffraction peaks in the XRD patterns of samples 1, 2, and 3 belonged to the characteristic peaks of $PbSO_4$ and $Pb_2(SO_4)O$ phases. In addition to $Pb_2(SO_4)O$, the characteristic peaks of $Pb_{10}(SO_4)Cl_2O_8$ [$Pb(SO_4)$ + $PbCl_2$ + 8 PbO] phase were identified in the XRD pattern of sample 4. The presence of Cl ions in the structure of $Pb_{10}(SO_4)Cl_2O_8$ phase caused a shift in the major diffraction peaks to the left-hand side of the XRD pattern of sample 4 compared to the major diffraction peaks of $Pb(SO_4)$ and $Pb_2(SO_4)O$ phases in the other XRD patterns. CdS and ZnO were identified in all samples as Cd- and Zn-containing phases, respectively. SEM photomicrographs of the deposited salt mixtures in Figures 6(a) through (d) show the morphology of the different available phases in samples 1, 2, 3, and 4, respectively. Spatial distribution of Zn, Pb, O, and Cd in the sample 2 can be seen in Figures 6(e) and (f). X-ray mapping, EDX analysis, and ICP/AAS (Table IV) results confirmed the presence of Fe in all the samples, although no Fe-containing phases were detected in the XRD patterns (Figure 5). Based on the EDX analysis results, Fe mainly dissolved in the Zn-rich regions. For example, in Figure 6(e), the Zn-rich regions contain 4.22 wt pct Fe in addition to 62.46 wt pct Zn, 8.65 wt pct Pb, 23.91 wt pct O, and 0.76 wt pct Cd. The Pb-rich regions in the same figure contain 63.44 wt pct Pb, 7.94 wt pct Zn, 1.52 wt pct Fe, 7.30 wt pct As, 3.01 wt pct Cd, 4.60 wt pct S, and 12.19 wt pct O.

DTA curves of samples 1 to 4 are presented in Figure 7. Except for the DTA curve of sample 1, a broad endothermic peak in the temperature ranges of 913 K to 1003 K, 923 K to 973 K, and 913 K to 1009 K
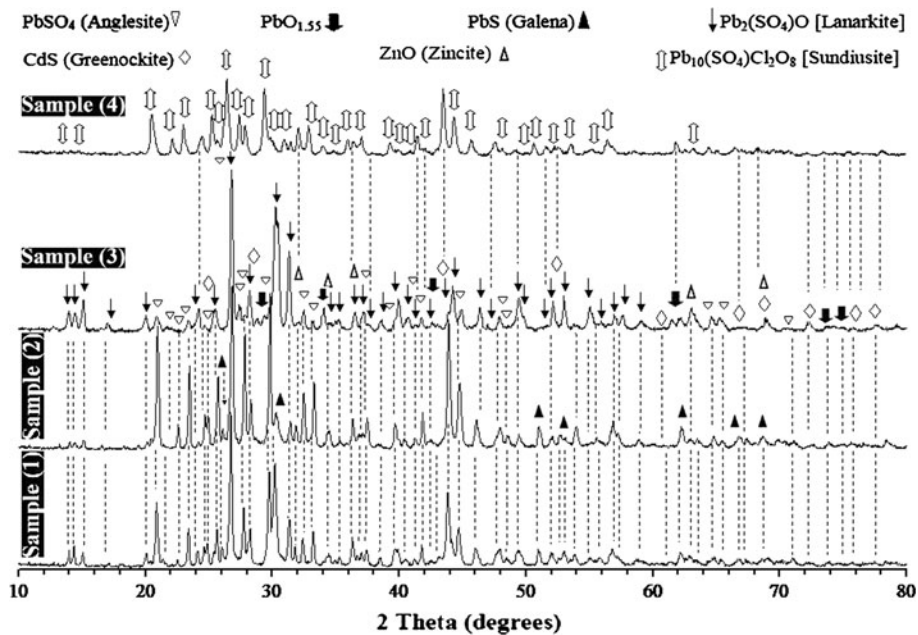
Fig. 5—XRD patterns of the deposited salt mixtures on the water wall tubes (HSS).

(640 °C to 730 °C, 650 °C to 700 °C, and 640 °C to 736 °C) was distinguishable in the DTA curves of samples 2, 3, and 4, respectively. These broad endothermic peaks were caused by heat adsorption due to the formation of a molten phase in the salt mixture. Accordingly, the formation of the molten phase occurred in the temperature range of 873 K to 973 K (600 °C to 700 °C) for samples 2 to 4. Therefore, the molten phase formed on the water wall at the operating temperature of the radiant boiler [973 K to 1103 K (700 °C to 830 °C)] due to the deposition of the salt mixtures. For sample 1, the DTA test was continued up to 1473 K (1200 °C). The presence of a few small endothermic peaks in the DTA curve of sample 1 in the temperature range of 1273 K to 1473 K (1000 °C to 1200 °C) indicated that the sample did not melt at temperatures less than 1273 K (1000 °C). Therefore, this sample did not contribute to the formation of the molten phase on the water walls, but it can still act as a thermal barrier against the heat transfer from the hot off-gas to the tubes. In the DTA curves of samples 2, 3, and 4, the inhomogeneous nature of the deposited salt mixtures caused the presence of several small endothermic peaks at temperatures higher than 973 K (700 °C). Furthermore, the physical appearance of the salt mixture after DTA test confirmed the formation of the molten phase for samples 2 to 4.

The presented DTA results clearly confirmed that the deposited salt mixtures have a strong tendency to form a molten phase at the operating temperature range of the radiant boiler. The fact of the matter is that precipitation of the molten salt phase on the water wall tubes was an important factor in exacerbating the corrosivity of the environment and accelerating the degradation of the tubes and the weld overlay alloy 625. The presence of the deposited salt mixtures, which caused the formation of the molten phase, can lead to the occurrence of

the molten salt-induced corrosion, also known as "hot corrosion," in the water wall (alloy 625 weld overlay + carbon steel tubes) of the radiant boiler, which will be discussed further in Section III–D. A reduction in the performance and reliability of the boiler during the operation is another consequence of the salt mixture deposition on the water walls because these deposited salt mixtures have a thermal insulation effect and can act as a thermal barrier against heat transfer between the hot off-gas and the tubes, as was mentioned previously.

It should be noted that the phase and the chemical characteristics of the actual deposits, gathered from the surface of the failed water walls, were considered to prepare a simulated salt mixture (see Table II) for conducting a hot corrosion study on the weld overlay alloy 625 in the laboratory scale. The main purposes of the laboratory-scale hot corrosion study were to assess the susceptibility of the weld overlay alloy 625 to the hot corrosion and to study the hot corrosion attack mechanism. It was not possible to use the actual deposits in the laboratory-scale hot corrosion study due to (1) safety concerns associated with the toxic and carcinogenic nature of the deposits (for example, the presence of As and Tl together with the high concentration of CdS in the composition of the deposited salt mixtures based on Table IV), (2) the inhomogeneous nature of the deposited salts, and (3) limitation in the amount of the available deposits. Therefore, it was essential to design a simulated salt mixture to be used as an electrolyte in the electrochemical tests. The phase and the chemical composition as well as the melting point of the simulated salt mixture were close to the characteristics of the actual deposits gathered from the surface of the failed water walls. As a result, it can simulate the corrosive condition of the boiler in the laboratory-scale hot corrosion tests to assess the susceptibility of the
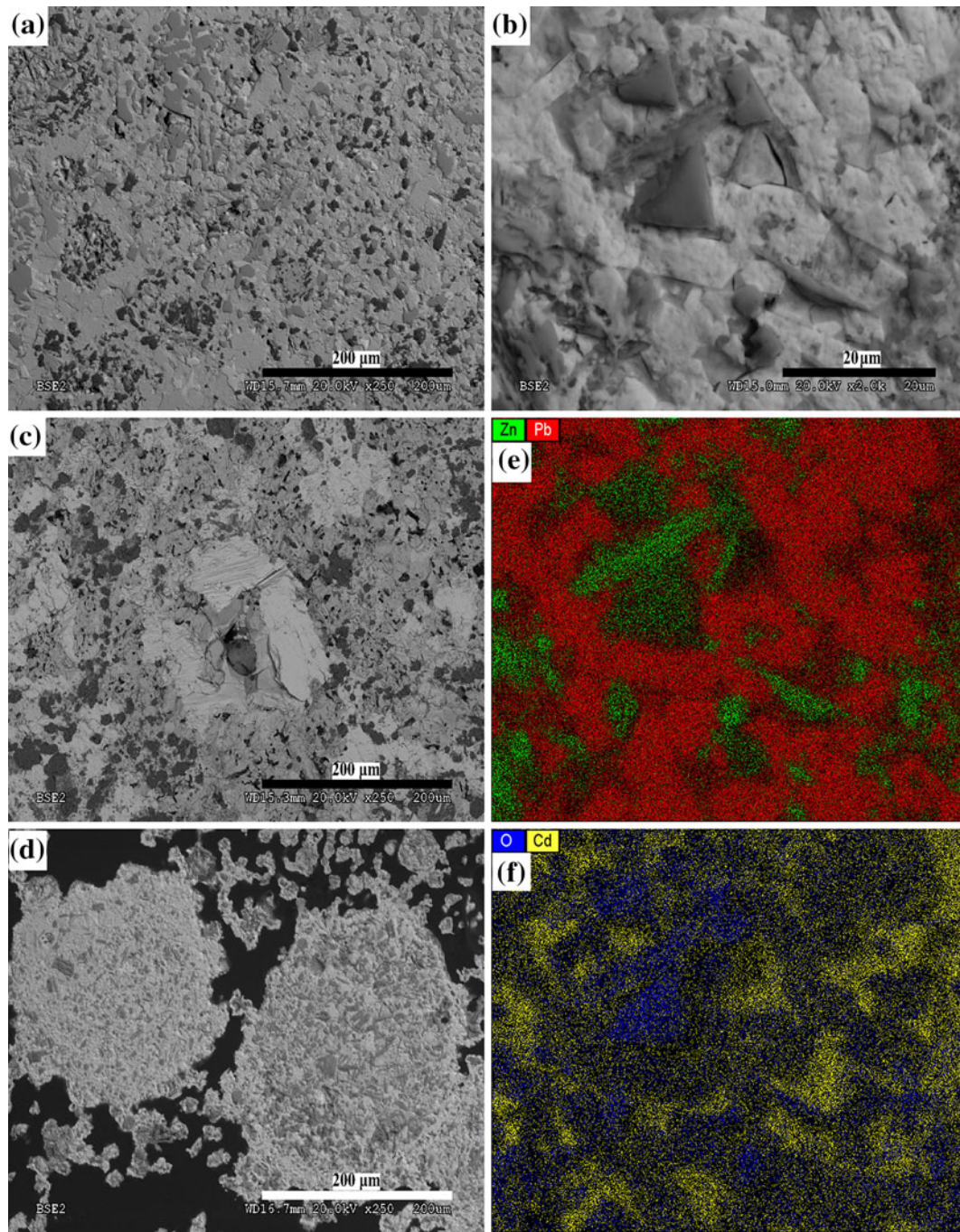
Fig. 6—SEM photomicrographs of the deposited salt mixtures on the water wall tubes: (*a*) sample 1; (*b*) sample 2; (*c*) sample 3; and (*d*) sample 4 as well as X-ray mapping of (*e*) Zn and Pb plus (*f*) Cd and O in sample 2.

unfailed weld overlay alloy 625 to the hot corrosion attack in a laboratory-scale study.

B. Microstructural Assessments

The microstructure of the alloy 625 in the as-welded conditions can be seen in Figure 4. Weld overlay alloy 625 exhibited a well-defined anisotropic, dendritic structure. A bright structure in the interdendritic regions pertained to the Laves phase. Prior to the visual inspection and the dye/fluorescent dye penetrant tests,

the surface of the failed sample (HSS) was cleaned from the deposits and carefully washed. During the visual examination, many cavities (pinholes) were observed on the HSS of the failed sample. These cavities were mainly detected in the boundaries of the deposited weld beads, as can be seen in Figure 2(b).

Except for the signs of the general corrosion (rust formation) which caused the reddish color of the CSS, there were no signs of failure or any abnormal features on the CSS constructed with the carbon steel. The occurrence of general corrosion on the CSS was

expected due to the weak corrosion resistance of the carbon steel. Welding defects such as excessive spatter, undercut, and porosity on the surface and cross section of the weld layer were detectable during the visual inspection of the weld overlay (see Figures 2(d) and 8). Based on the morphology of the porosities in Figures 8(a) through (c), (f), and (g), porosities formed because the shielding gas (Argon) was trapped inside the fused zone. The flow rate of the shielding gas during welding was 15.6 to 16.5 L per minute (33 to 35 cubic foot per hour, CFH). The excessive spatter and the undercut defects can be formed due to high heat input to the welding pool during the welding process.[20] The high heat input is a consequence of improper selection of arc power parameters (voltage and current) or low deposition rate of the weld metal (low filler metal feed rate). In

Figures 8(c) and (g), because of the molten salt penetration into the weld defect, the carbon steel substrate is directly exposed to the penetrated molten phase and the occurrence of the hot corrosion attack (sulfidation and oxidation of Fe, based on the EDX results in Figure 15) in the carbon steel tube can be observed. Further details will be discussed in Figures 15 and 16.

The chemical composition of the carbon steel tube and filler metal, determined by the ICP/AAS, is presented in Table I. The dilution level was determined based on the concentration of Fe in the weld overlay, the filler metal, and the carbon steel tube (base metal). For simplification, it can be assumed that the fusion zone was fully mixed. Accordingly, the final weld composition will be a mixture of the carbon steel substrate and the filler metal, which can be calculated by applying the following equation[21,22]:

$$C_{fz} = C_{fm}(1 - D_{Fe}) + C_s(D_{Fe}) \Rightarrow D_{Fe} = \frac{C_{fz} - C_{fm}}{C_s - C_{fm}} \quad [1]$$

where C_{fz}, C_{fm}, and C_s are the concentration of Fe in the fusion zone, the filler metal, and the carbon steel substrate, respectively, and D_{Fe} is the dilution level of Fe. Based on Eq. [1], the dilution level of Fe was equal to 23.62 pct. The thickness of the tubes in CSS (no weld overlay on this surface) was equal to 5 mm, the same as the thickness of the tubes originally used for construction of the water walls. The thickness of the tubes was reduced to 2.12 ± 0.3 mm in the HSS. As a result, the total reduction in the tube thickness in the HSS was about 2.88 mm. Based on Eq. [2],[21,22] for geometric dilution calculation, 1.04 mm of the reduction in the thickness of the tube was attributed to the dilution and the rest of the reduction in the thickness (~1.84 mm) was attributed to the degradation of the tubes prior to applying the weld overlay alloy 625 for protection. A good agreement and consistency between

Table IV. Chemical Composition (Weight Percent) of the Deposited Salt Mixture on the Water Wall Tubes

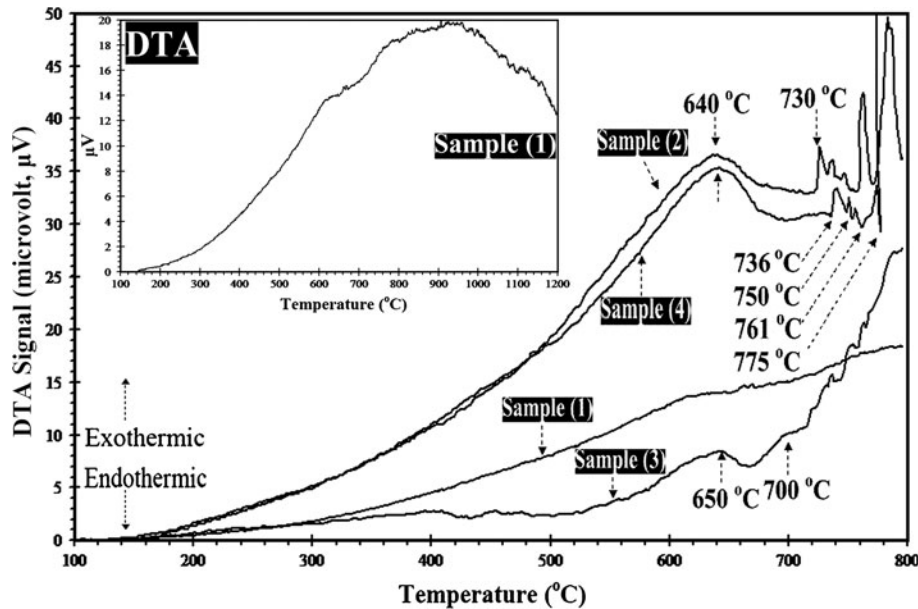|	Sample 1	Sample 2	Sample 3	Sample 4
Pb	48.93	44.26	52.01	39.91
Zn	11.56	10.94	8.74	10.05
Cd	8.54	11.58	4.13	14.14
Fe	2.65	2.00	3.70	1.24
K	0.41	0.49	0.19	0.44
Na	0.10	0.12	0.07	0.09
Ag	0.2	0.16	0.08	0.15
Cu	0.2	0.16	0.35	0.12
As	0.86	0.69	0.69	0.35
Sb	0.18	0.16	0.32	0.12
Cl	1.02	2.27	1.51	2.50
S	5.98	6.98	5.28	7.61
Si	1.76	1.31	2.88	1.05
Sn	0.25	0.19	0.13	0.11
In	0.15	0.13	0.14	0.06
Tl	0.07	0.78	<0.01	0.38

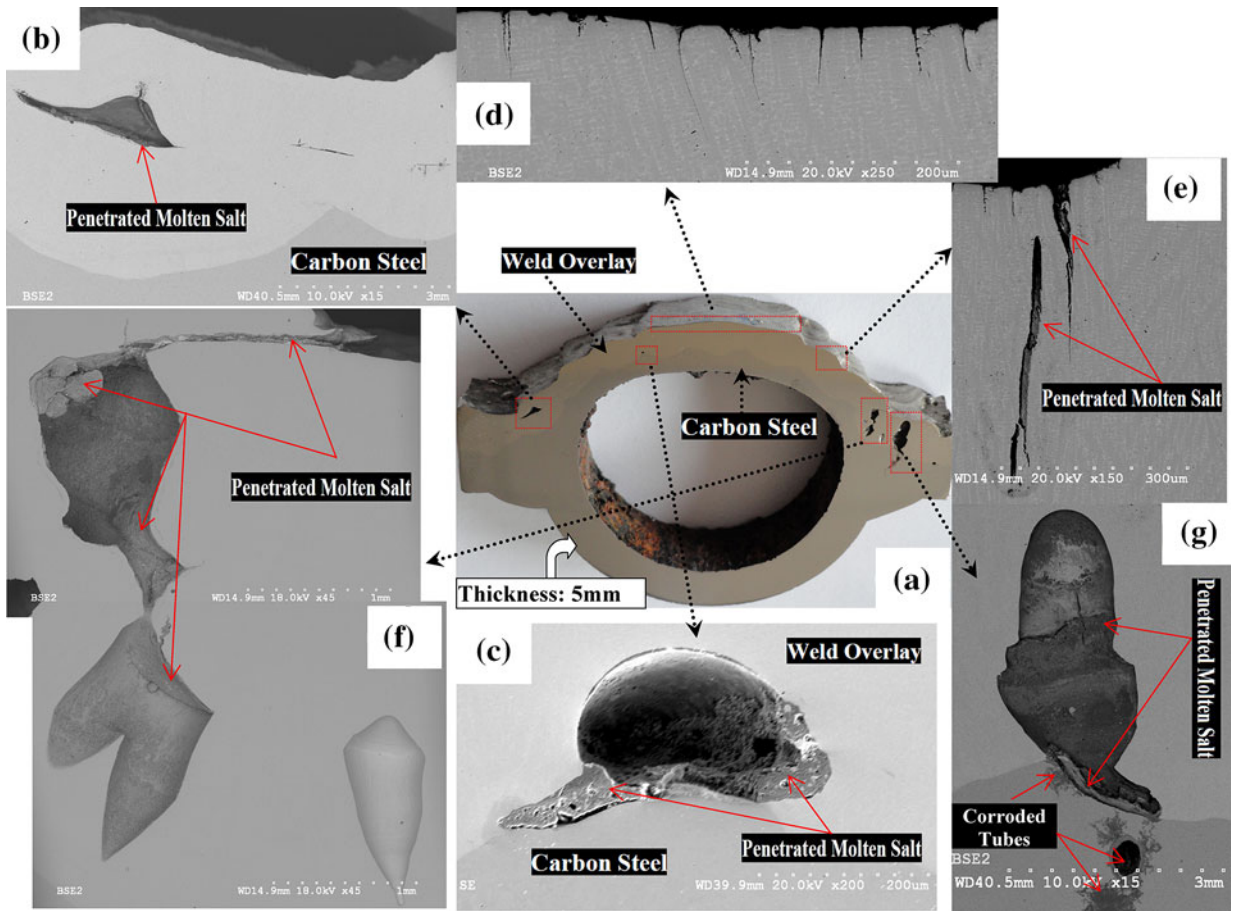Fig. 7—DTA curves of the deposited salt mixtures on the water wall in the radiant boiler.

Fig. 8—Cross-sectional SEM photomicrographs from a section of the failed overlaid tubes after polishing.

the obtained dilution levels through the geometric measurements and the chemical analysis method was reported in the literature.[21,22] Equation [2] is as follows:

$$D_{Fe} = \frac{A_s}{A_s + A_{fm}} \qquad [2]$$

where A_s and A_{fm} are the area of the melted substrate and the melted filler metal, respectively, and D_{Fe} is the dilution level of Fe. When a section of the weld overlaid tube is considered to have a width of one unit of length (cm or mm), the section of the weld overlay will be rectangular in shape. Under this condition, Eq. [2] will be the ratio of the melted substrate thickness (T_s) to the total melted cross-sectional thickness from the filler metal and substrate ($T_s + T_{fm}$). The cross-sectional thickness of the filler metal was equal to 3.38 mm (T_{fm} = average thickness of the weld overlay).

An increase in the dilution, due to the high heat input and the arc power, caused a significant decrease in the thickness of the substrate (tube) because the tube metal (carbon steel) melted at the welding temperature (see Figures 2(d) and 8(a)). In Figures 2(d) and 8(a), the observed considerable distortion (plastic deformation) in the tube wall under the weld layer clearly confirmed the excessive heat input to the base metal during the depositing of the weld overlay by the GMAW technique;

consequently, a significant amount of Fe was transferred to the weld overlay from the carbon steel tube. Although the concentration of Fe in the alloy 625 consumable electrode, used for deposition of the weld overlay through the GMAW technique, was 0.383 wt pct, the concentration of Fe in the weld overlay chemical composition was significantly higher, 23.64 wt pct (Table I), as a direct consequence of the dilution phenomenon and the high heat input/arc power. The concentration of C and Si in the alloy 625 consumable electrode (filler metal) was equal to 0.008 and 0.072 wt pct, respectively, but the dilution from the carbon steel substrate caused an increase in the C and Si content of the weld overlay. The amount of C and Si in the weld overlay alloy 625 was equal to 0.05 and 0.3 wt pct, respectively (Table I). These amounts of C and Si in the weld overlay alloy 625 can significantly increase the susceptibility of the weld alloy to the occurrence of fusion zone solidification cracking during the welding process.[23–26] Reportedly, solidification cracking susceptibility of the weld overlay alloy 625 increases with increasing the dilution level.[21] Other studies confirmed that the content of Fe in the weld overlay alloy should be kept to less than 6 to 7 pct to minimize the adverse effects of Fe on the properties of the deposited weld layer and its corrosion resistance.[27,28] Based on the studies of Adamiec,[28] for alloy 625 weld overlay on the

tubes of 1.0305 steel with a GMAW process, a heat input rate (linear energy of pad welding) less than 300 kJ/m is required in order to keep the Fe concentration in the weldment less than 7 pct by controlling the dilution. However, in the case of the current study, the maximum heat input rates for the GMAW process and the GTAW wash pass were about 600 and 700 kJ/m, respectively. These values were significantly higher than the optimum heat input rate suggested by Adamiec.[28] This is evidence to confirm the adverse effect of inappropriate selection of the heat input rate in the GMAW process on the dilution and high concentration of Fe in the weldment. Shielding gas flow rate in the GMAW process, applied in a radiant boiler, (15.6 to 16.5 L per minute), was almost the same as the value reported by Adamiec (18 L per minute).[28]

Overall, two factors including (1) the solidification temperature range, the range over which the solidification cracking occurs, and (2) the amount of the secondary phase, which forms at the terminal stage of solidification, control the relationship between the dilution phenomenon and the solidification cracking susceptibility.[25] It has been well established that higher contents of C, Si, and particularly Nb, in alloy 625 simultaneously increase the solidification temperature range of the alloy and reduce its liquidus/solidus temperature. These two factors raise the susceptibility of the weld overlay alloy 625 to the solidification cracking during welding and reduce the weldability (resistance to solidification cracking) of the alloy.[23,25] Furthermore, excessive amounts of C, Si, and Nb in alloy 625 can promote the termination of the solidification process by a eutectic-like reaction between the gamma phase (γ) with FCC crystallographic structure and various Nb-rich phases and/or Laves. It causes further increase in the solidification temperature range and, thus, raises the tendency for the fusion zone solidification cracking in the alloy 625 weld overlays.[21,24,25] According to Dupont et al.,[21] for weld overlay alloy 625, a higher content of Mo- and Nb-rich secondary phases, Laves, in the interdendritic regions means that higher amounts of Mo and Nb-rich liquid phase formed at the final stage of solidification of the weld overlay, which wet the grain boundaries as a continuous film. Consequently, shrinkage strain across the boundaries, which cannot be accommodated, causes the separation of the boundaries, which results in the formation of the cracks as terminal eutectic liquid solidifying.[21,29,30]

Cross-sectional SEM photomicrographs of the weld overlay samples can be seen in Figures 9(a) through (d). Based on the EDX results, the white areas (Laves) were rich in Mo and Nb. Greater concentration of Mo and Nb in the Laves phase, compared to the bulk composition or γ matrix, was also reported by Maguire and Michael.[29] These areas appeared in the interdendritic regions. The chemical composition as well as the spatial distribution of Mo, Nb, and Ni in this region will be discussed in Figure 10 and Table V based on the EDX and X-ray mapping results. The formation of solidification cracks and cavities along these regions and the interdendritic nature of solidification cracking are

evident in Figures 9(c) and (d). The pores can act as stress-raiser zones to facilitate the crack formation in the weld layer during service or the pathways for penetration of corrosive species well inside the layer to accelerate the degradation of the alloy. This confirmed that the interdendritic regions are susceptible to the solidification cracking. Solidification cracks were found to be associated with these regions in the weld overlay alloy 625 mainly due to the segregation of Mo and Nb into these regions and formation of the Laves constituent during solidification. Formation of pores in the interdendritic regions of the weld overlay alloy 625 and direct effect of porosities on the crack formation and subsequent enhanced corrosion penetration into the alloy were also reported by Kalivodova et al.[6] The mechanism of solidification crack formation in interdendritic regions of weld overlay alloy 625 has been clearly described elsewhere.[21] Formation of solidification cracks in Mo- and Nb-rich interdendritic regions was also reported by Dupont.[25]

The SEM photomicrograph in Figure 9(e) shows the presence of large inclusions in the microstructure of the weld layer. EDX elemental analysis in Figure 9(f) indicates that the inclusions were rich in Fe, Ni, Cr, and O. The concentration of Fe, Ni, Cr, and O in the inclusions was about 50.29, 18.61, 17.25, and 7.61 wt pct, respectively. High concentration of Fe in the inclusions was due to dilution. Based on this, inclusions were susceptible to corrosion and dissolution when the weld overlay was exposed to the corrosive environment. In Figure 9(e), a microcrack, initiating from the edge of the inclusion, is shown by an arrow. Inclusions can act as stress-raiser zones to accelerate the initiation and propagation of the cracks in the weld overlay during service. As was mentioned previously, a mechanical hammer was periodically used in the radiant boiler to hit the water walls, which caused the physical removal of the deposited salt on the water walls to facilitate the heat transfer through the tubes. Crack initiation and propagation in the weld overlay can be facilitated by this externally applied stress. Moreover, the role of the deposited salts on the water walls in inducing the thermal stresses in the weld layer should be considered. Deposited salts on the water walls insulated the hot off-gas from the water coolant circulating inside the tubes. A thick layer of the deposited salts acted as a thermal-resistant barrier against the heat transfer in the tube's wall; consequently, thermal stresses were induced in the weld layer. In fact, non-uniform distribution of the temperature on the water walls and formation of hot and cold zones on the weld overlay, due to the partial deposition of a thick layer of the salt mixtures, caused expansion and contraction of the weld overlay, which can directly contribute to inducing the thermal stresses. These sources of stress in the weld overlay can contribute to facilitating the crack initiation and propagation in the weld layer, in particular from the zones which acted as stress raisers such as cavities and inclusions. Studies confirmed that the thermal expansion coefficient of alloy 625 is very close to that of carbon steel, which keeps the weld layer well adhered to the tubes even after being in service for a long time.[31] Furthermore, weld overlay is
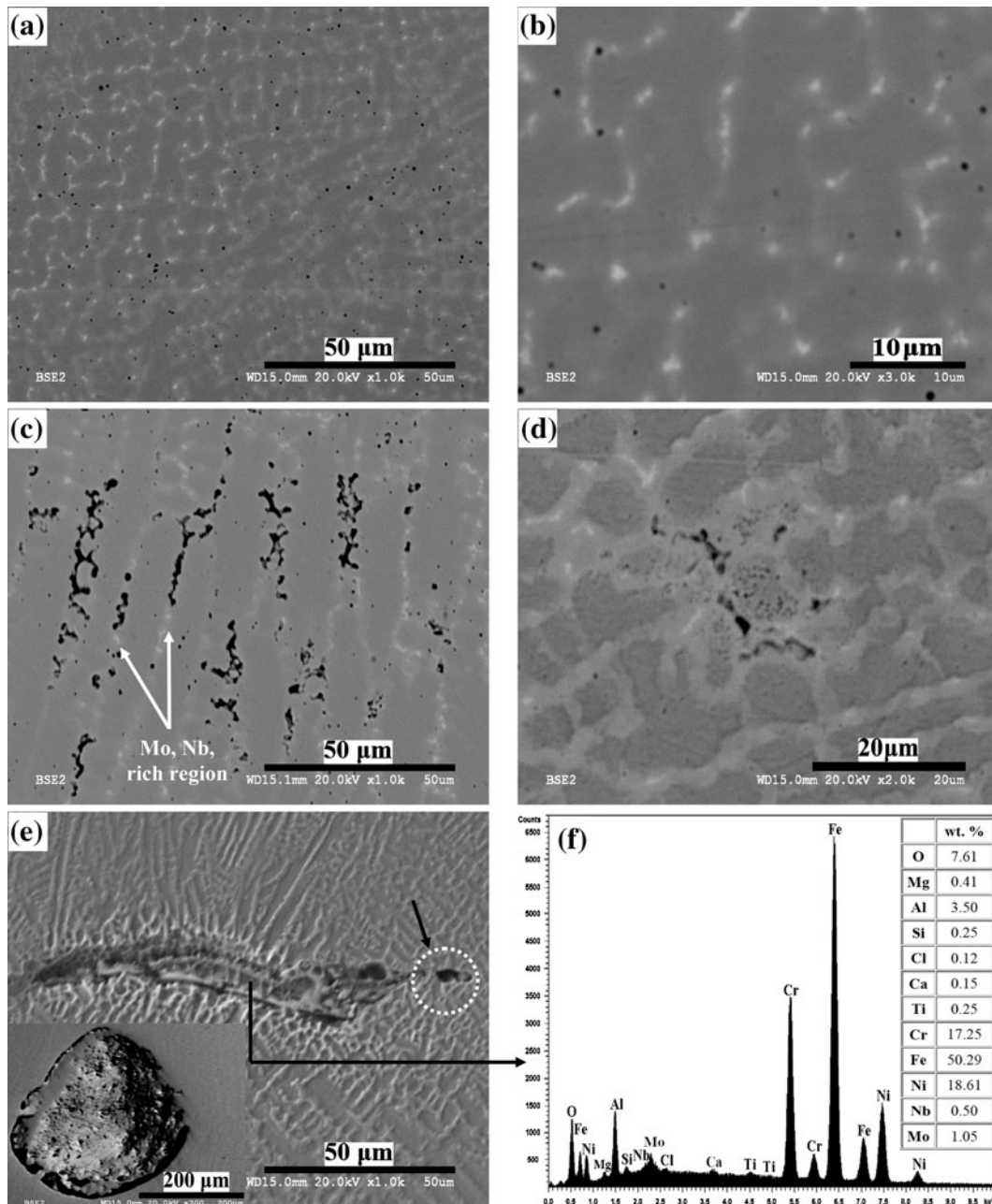
Fig. 9—Cross-sectional SEM photomicrographs of the weld overlay alloy 625 which show (*a*, *b*) microsegregation in the dendritic regions and formation of the Laves; (*c*, *d*) solidification cracking; (*e*) Fe-rich inclusion; and (*f*) EDX elemental analysis of the Fe-rich inclusion.

found to be under compressive stress, lower than the alloy's yield stress, during normal operating temperature transient in the boiler.[32] Because of these two factors, alloy 625 is highly resistant to stress corrosion cracking (SCC) and thermal fatigue under the normal working conditions of the boiler.[31]

SEM/EDX and X-ray mapping results in Figure 10 clearly show the microsegregation of Mo and Nb into the interdendritic region of the weld overlay and formation of the Laves constituent during non-equilibrium solidification of the weldment. X-ray mapping results showed the depletion of Mo (5.51 ± 1.10 wt pct) and Nb (1.91 ± 0.70 wt pct) in the dendrite cores, compared to

the Mo (11.88 ± 0.67 wt pct) and Nb (12.11 ± 0.95 wt pct) content of the interdendritic regions. EDX elemental analysis of the dendrite cores and interdendritic regions in Table V confirmed the excessive amounts of Mo and Nb in the interdendritic regions. Compared to Cr, Mo, Fe, and Si elements, the strongest tendency to partition to the interdendritic regions pertained to Nb. Based on the EDX results and X-ray mapping of Ni in Figure 10, dendrite cores were enriched with Ni and Fe. The EDX results shown in Table V confirmed that Cr concentration in the dendrite cores (18.94 ± 0.61 wt pct) is higher than interdendritic regions (16.86 ± 0.37). This confirmed the tendency of Cr for microsegregation in the weld overlay
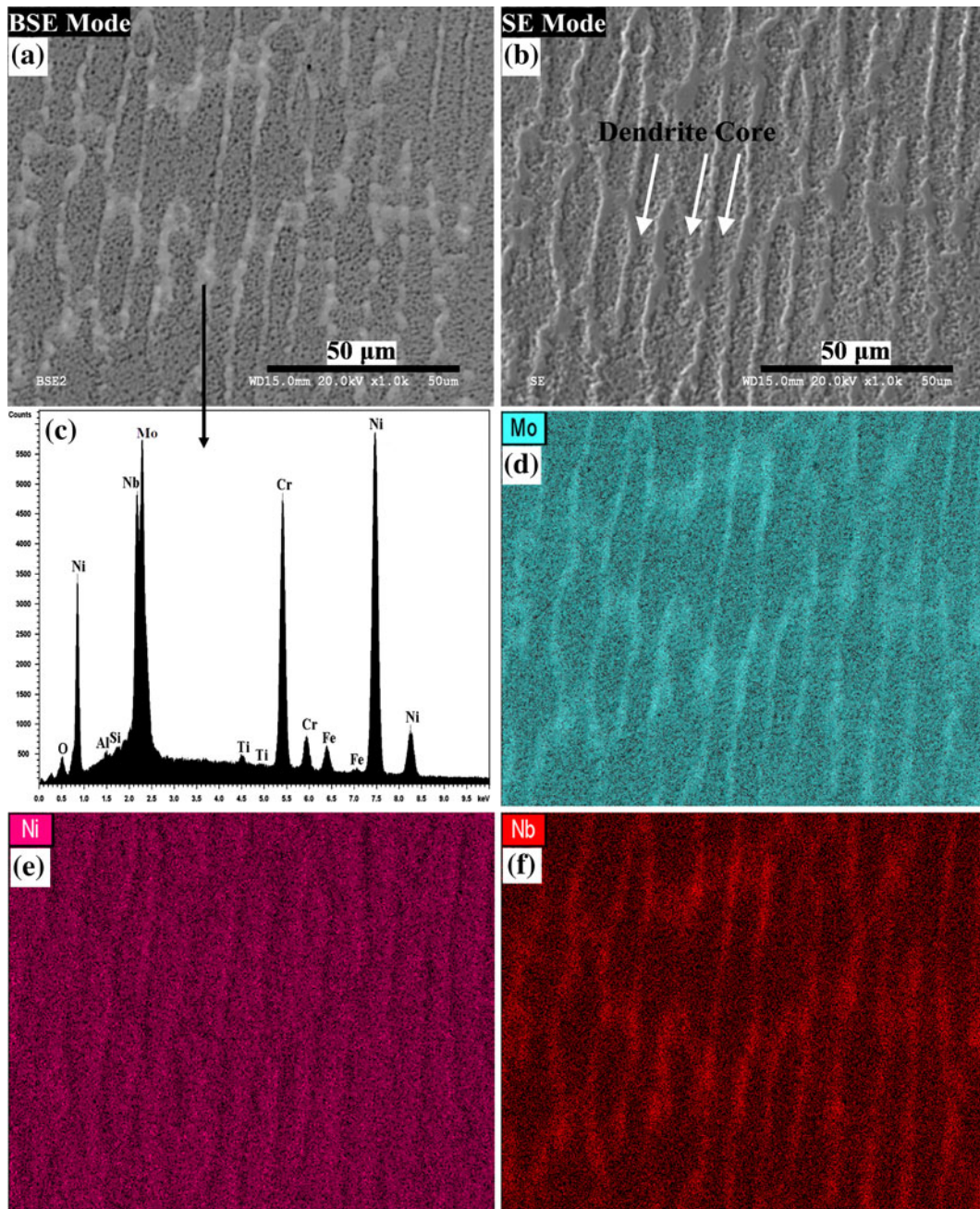
Fig. 10—Cross-sectional SEM photomicrographs of the weld overlay alloy 625 in (*a*) BSE and (*b*) SE mode as well as (*c*) EDX elemental analysis of the Laves phase and X-ray mapping of (*d*) molybdenum; (*e*) nickel; and (*f*) niobium in the dendritic structure.

dendritic structure. The tendency of Si for microsegregation to the interdendritic regions was evident based on the presented results in Table V. Si is known as an element that strongly promotes the Laves formation.[26] Therefore, rejection of Si from the solidified γ phase dendrites to the interdendritic liquid phase during the solidification process of the weld overlay alloy 625 can promote the formation of the Laves in the interdendritic regions. Furthermore, high concentration of Fe in the weld overlay, as a consequence of dilution, can exacerbate the problem and increase the tendency for the Laves formation, thereby promoting the

γ/Laves constituent.[33,34] The measured concentration of Si in the Laves was 0.77 ± 0.08 wt pct (see Table V). These findings are in agreement with the findings of the previous studies.[21,25,26] Cr is one of the most effective alloying elements in alloy 625 to act against corrosion, necessitating at least 18 to 24 wt pct to optimize its effectiveness.[1,33–35] Therefore, determined concentrations of Cr (16.86 ± 0.37) in the interdendritic regions of the weld overlay were slightly below the acceptable range and this can adversely affect the corrosion resistance of the weld overlay. Dupont *et al.* reported that the tendency of Mo and Nb to segregate

Table V. EDX Elemental Analysis (Weight Percent) from the Dendrite Cores and the Interdendritic Regions of the Weld Overlay Alloy 625

	Dendrite Core	Interdendritic Region
Nb	1.91 ± 0.70	12.11 ± 0.95
Mo	5.51 ± 1.10	11.88 ± 0.67
Ni	54.89 ± 2.11	45.61 ± 1.14
Cr	18.94 ± 0.61	16.86 ± 0.37
Fe	16.19 ± 3.24	10.02 ± 0.52
Ti	0.19 ± 0.09	0.33 ± 0.14
Si	0.22 ± 0.18	0.77 ± 0.08
Al	0.11 ± 0.05	0.12 ± 0.02
O	2.05 ± 0.59	2.41 ± 0.15

increases as a consequence of transferring Fe to the fusion zone due to the dilution, which means that the solubility of Mo and Nb in gamma phase (γ) decreases with increasing the dilution level of Fe.[21,25,26] Accordingly, more Mo and Nb are rejected from the solidified γ phase to the liquid phase during solidification. When this solute-rich liquid solidifies between the dendrites, microsegregation occurs in the interdendritic regions.[21,25,26] Based on these findings, in the present study, segregation of Mo and Nb into the interdendritic region of the weld overlay during solidification can be justified considering the excessive content of Fe (23.64 wt pct) in the weld overlay. This can justify why the dendrite cores were depleted in Nb and Mo while they contained a higher concentration of Fe compared to the interdendritic regions. The segregation phenomenon plays an important role when weldability and solidification of weldment are concerned. Because of the segregation phenomenon, the core of the dendrite arms contained less solute than the interdendritic regions in the weld overlay alloy 625, which caused the higher solidus temperature of the dendrite arms. Segregation can also have a detrimental effect on the mechanical properties of the weldment.[36] The morphology of the Laves phase in Figures 9 and 10 can show that the solute-rich liquid, which solidified at the terminal stage of solidification, had a propensity to spread out as a continuous thin film between the dendrites because of having a low surface tension.[37]

When Mo and Nb segregate from the solidified phase to the liquid phase during welding solidification, the low diffusion rate of these two elements in the γ phase prohibits them from diffusing back to the dendrite cores.[21,26,38] In other words, solid-state diffusion of substitutional alloy elements, such as Mo and Nb, in alloys with FCC crystallographic structure, such as alloy 625, is negligible under typical cooling rates of arc welding.[21,26,39] For this reason, it is plausible to claim that the determined concentrations of substitutional alloying elements in Table V are very close to the concentration of the alloying elements at the onset of solidification of the weld overlay. In addition to the Cr and Ni concentration gradient, a concentration gradient of Mo and Nb between the dendrite cores and the interdendritic regions also formed, confirmed by X-ray mapping (Figure 10) and EDX results (Table V). The concentration gradient of Mo and Nb adversely affected the corrosion resistance of the weld overlay and made the weld alloy susceptible to the preferential corrosion in the Mo- and Nb-depleted dendrite cores due to the galvanic effect. Based on the literature,[6,40] poor resistance to localized corrosion in the weld metal, due to the segregation of Mo and Nb alloying elements, can lead to the failure of the weld overlay alloy during service in power plants. It should be noted that the role of Mo in alloy 625 is to make the alloy resistant to crevice and pitting corrosion when it is uniformly distributed in the alloy.[1] From a corrosion perspective, depletion of Cr and Ni in the Mo- and Nb-rich interdendritic regions can reduce the resistance of these regions to corrosion attack. As was mentioned earlier, increasing the dilution level and the concentration of Fe in the weld overlay exacerbated the microsegregation of Mo and Nb in the dendritic structure of the weld overlay[21]; consequently, the concentration gradient of Mo and Nb and the susceptibility of the dendrite cores to the preferential corrosion increased. Dupont *et al.*[21] mentioned that the segregation potential of Nb and Mo in the weld overlay, which depends on the Fe concentration, is indirectly affected by the arc power and volumetric filler metal feed rate because these welding parameters control the dilution level and chemical composition of the weld layer, in particular the concentration of Fe in the weld overlay. The direct effect of processing parameters of arc power and volumetric filler metal feed rate on the dilution level was also investigated by Banovic *et al.*[22]; it was found that an increase in the volumetric filler metal feed rate and/or a decrease in the arc power can reduce the volumetric melting rate of the substrate and, thus, the resultant weld metal dilution level.

The solidification sequence of an alloy 625 weld overlay deposited on 2.25Cr-1Mo steel by GMAW was explained elsewhere in detail.[25] In summary, γ dendrites form at the early stage of solidification, and depletion of Mo and Nb occurs at the dendrite cores due to the low solubility of these two elements in γ phase (particularly in the presence of Fe) while Fe, Ni, and Cr segregate to the solidifying γ dendrites.[25] By continuation of the solidification, the concentrations of Mo and Nb increase at the interdendritic liquid phase until the final stage of the solidification in which termination of solidification occurs by a eutectic-like reaction between γ phase and Laves.[25] Based on this report, the presence of Fe and Si promotes the formation of Laves phase during solidification of weld overlay alloy 625.[25] This mechanism was consistent with the presented results in Figures 9 and 10 and Table V. NbC or other Nb-containing carbides were not detected in the weld overlay microstructure in the current study, which can be justified considering the low concentration of C in the weld overlay (see Table I). This observation can confirm that the eutectic reaction between γ phase and the Laves is the terminal stage of solidification in the alloy 625 weld overlay.

The measured microhardness values of the weld overlay alloy 625 samples were in the range of 325 to 369 HV100. This range of microhardness values means that no annealing or age hardening occurred in the weld during service in the boiler environment.[41] Cortial *et al.*[41] reported that heat treatment for 8 hours at 1273 K (1000 °C) causes the concentration gradient and heterogeneity between the interdendritic regions and

dendrite cores to vanish in alloy 625 weld overlay on A533 steel plates by means of the TIG welding process. In other words, this heat treatment procedure can make the welding structure fully homogenized and dissolve the detrimental Laves phase, thereby improving the corrosion resistance of the weld overlay.[41] However, this approach, heat treating the weld overlay at 1273 K (1000 °C) for 8 hours, is not practical in solving the issue of concentration gradient of Ni, Cr, Mo, Nb, Fe, and Si in the weld overlay alloy 625, where the welding procedure is done on-site in the boiler.

Overall, the dilution and, consequently, the presence of a significant amount of Fe in the chemical composition of the weld overlay alloy 625 are the key issues in the water walls. Dilution is the root cause of exacerbating the susceptibility of the weld layer to solidification cracking. It also makes the dendritic structure of the weld layer susceptible to preferential corrosion due to the microsegregation of Mo and Nb from the dendrite cores to the interdendritic regions, causing the formation of Mo- and Nb-depleted zones and Laves phase. Therefore, it is critical to pay attention to the relation between the dilution and the welding parameters to understand how the welding parameters should be optimized to minimize the dilution, reducing the solidification cracking susceptibility. Processing parameters of arc power (current and voltage) and filler metal feed rate control the volumetric melting rates of the filler metal and substrate and, thus, weld metal dilution.[21,22] In fact, by decreasing the arc power/heat input and increasing the volumetric filler metal feed rate (deposition rate), which means maximizing filler metal feed rate-to-arc power ratio, the dilution level and Fe content in the overlay will be minimized. This can ultimately lead to improving the cracking resistance of the weld overlay and its corrosion resistance and avoid the formation of undesirable phases and inclusions.[6,22,25,42] An optimum heat input is important not only to reduce the dilution and segregation level of the major alloying elements of the alloy but also for providing sufficient wetting for a good weld to be preceded.[6] Reportedly, in addition to minimizing the heat input, a high weld metal cooling rate has to be used to decrease the Nb segregation and amount of detrimental Laves phase, thereby reducing the susceptibility of the occurrence of the solidification cracking.[30,36] A direct current with reverse polarity (DECP) was used in the GMAW process to apply the weld overlay on the water walls of the radiant boiler. However, studies showed that the use of a pulsating current with a stable power voltage can provide a higher quality weld layer.[28] The use of the pulsing technique in welding is a beneficial strategy to reduce the heat buildup during the process.[36] Accordingly, it is recommended to use a pulsating direct current for applying weld overlay to control segregation and dilution phenomena in the weldment, thereby reducing the susceptibility to the solidification cracking. Compared to the straight direct current, residual stress and distortion are reduced due to the lower heat input by applying a DC pulsating current.[43]

The relatively large dendritic arm spacing of the weldment in Figures 4(c) through (e) can be evidence of the slow weld cooling rate of the weldment during applying the weld overlay alloy 625 by the GMAW technique. The weld cooling rate can strongly affect the segregation because it is a time-dependent phenomenon.[36] Studies by Radhakrishna and Prasad Rao[36] have shown that coarse dendritic spacing provides congenial/preferential sites for segregation during solidification of the weld metal. Circulating water inside the tubes during the deposition of the weld layer is an effective option to increase the cooling rate of the weldment and to reduce the microsegregation and Laves formation. This is an important technical consideration where applying weld overlay on the water walls of a boiler is concerned. Studies confirmed that forced internal cooling of the tubes can ensure appropriate weld layer quality and appropriate Fe content on the surface of the weld layer.[28]

Selecting a filler metal with a relatively high content of C and low content of Si and Fe to promote the formation of γ/NbC at the terminal stage of the overlay solidification at the expense of the γ/Laves is another precaution for decreasing the solidification temperature range and, therefore, reducing the cracking susceptibility.[23,25] Based on the literature,[36,44] it is generally believed that Laves is a phase in the form of (Ni, Fe, Cr)$_2$(Nb, Mo, Ti, Si) with a hexagonally close packed crystallographic structure. The inherent brittle nature of the intermetallic Laves phase causes them to act as preferential sites for crack initiation and propagation in the weld overlay structure,[36,44] as confirmed by Figure 9. It is pertinent to mention here that, based on the presented results in Table I, the effect of Fe and the dilution on making the overlay susceptible to the solidification cracking is predominant in the case of the current study. Accordingly, maximizing filler metal feed rate-to-arc power ratio looks to be more effective for reducing the cracking susceptibility.

C. Molten Phase Penetration into the Weld Overlay

After visual inspection, dye penetrant and fluorescent dye penetrant tests were conducted on the HSS of the failed water wall to reveal cracks and discontinuities which are open to the HSS. These defects might not be detectable through a normal visual inspection. In the boiler environment, the weld layer was partially covered by the deposited salt mixtures, characterized in Section III–A. The results of the dye penetrant and fluorescent dye penetrant tests can be seen in Figure 11. In Figures 11(a) through (c), a dye penetrant test reveals the presence of the cavities (pinholes) with various diameters as well as many discontinuities between the weld beads. The cavities mainly appeared in the boundaries of the weld beads. As can be seen in Figure 11(c), the dye penetrant test did not reveal the presence of any cracks on top of the deposited weld bead, on the crown of the tube, but results of the fluorescent dye penetrant test confirmed the presence of the cracks in this area. The dye penetrant test did not successfully reveal the presence of such cracks in other regions of the weld overlay because of the limitation of the discontinuities and crack sizes, which can be detected by the dye penetrant test. For more accurate results, a fluorescent
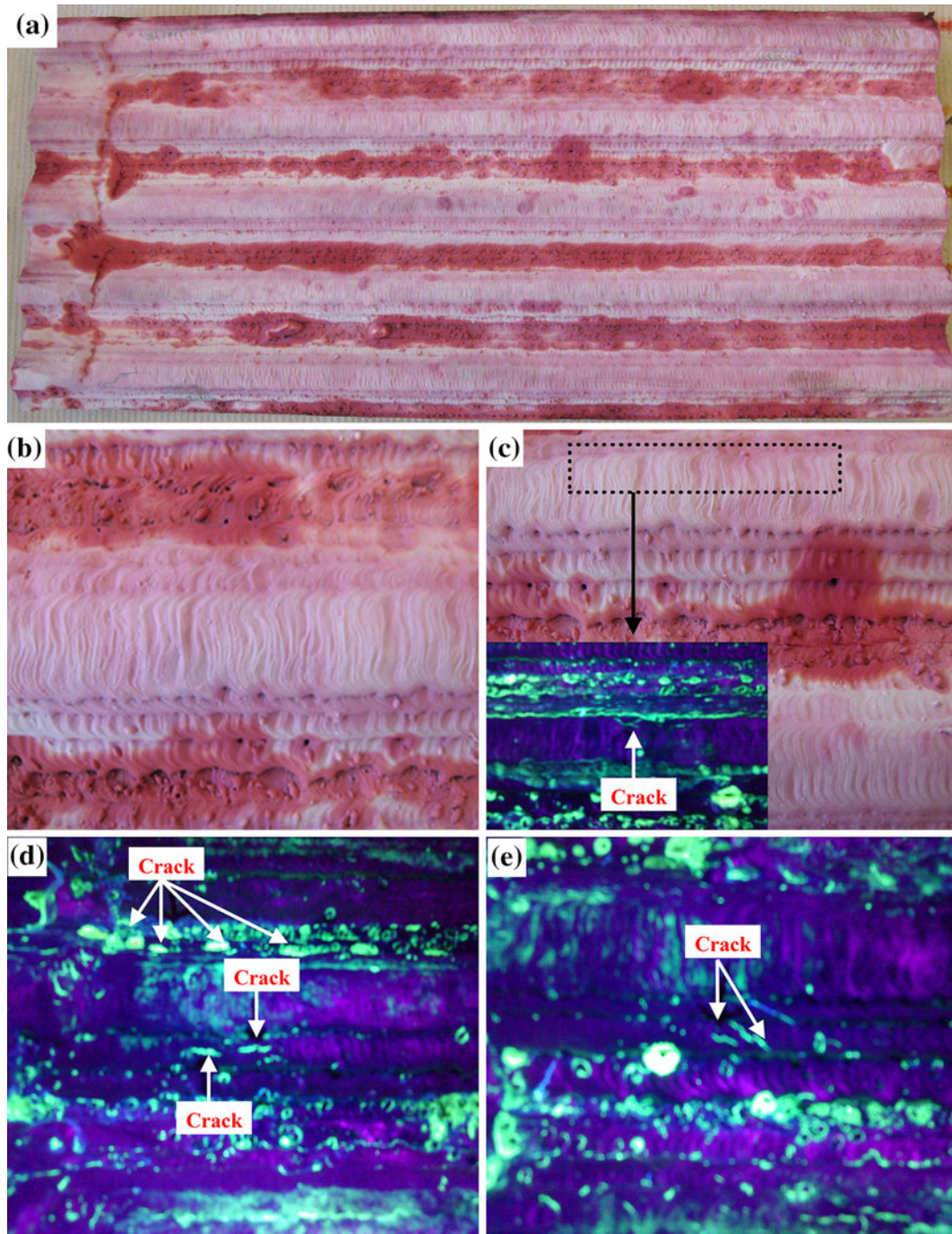
Fig. 11—The surface of the weld overlay after applying dye penetrant [(a) to (c)] and fluorescent dye penetrant test (d, e).

dye penetrant test, as a more sensitive test for crack detection, was conducted on the HSS. The results are presented in Figures 11(c) through (e). As was expected, the fluorescent dye penetrant test revealed the presence of some cracks which were not identifiable by the dye penetrant test. Conducting visual inspection and dye/fluorescent dye penetrant tests assisted in determining the suitable locations for cutting the metallographic samples. Despite the fact that the fluorescent dye penetrant test is more accurate than the dye penetrant test, it is not still precise enough to reveal all surface

cracks. For this reason, the entire surface of the weld overlay was also studied by SEM.

In Figures 12(a) through (c), the presence of a network of well-developed circumferential cracks across the HSS of the weld overlay is evident. During the SEM study, in some locations, it was clear that the subsurface region of the weld layer flaked off. A single well-developed, straight, and unbranched circumferential crack, which was located adjacent to the membrane and covered by the deposited salts, can be seen in Figures 12(d) through (f) from two different directions,
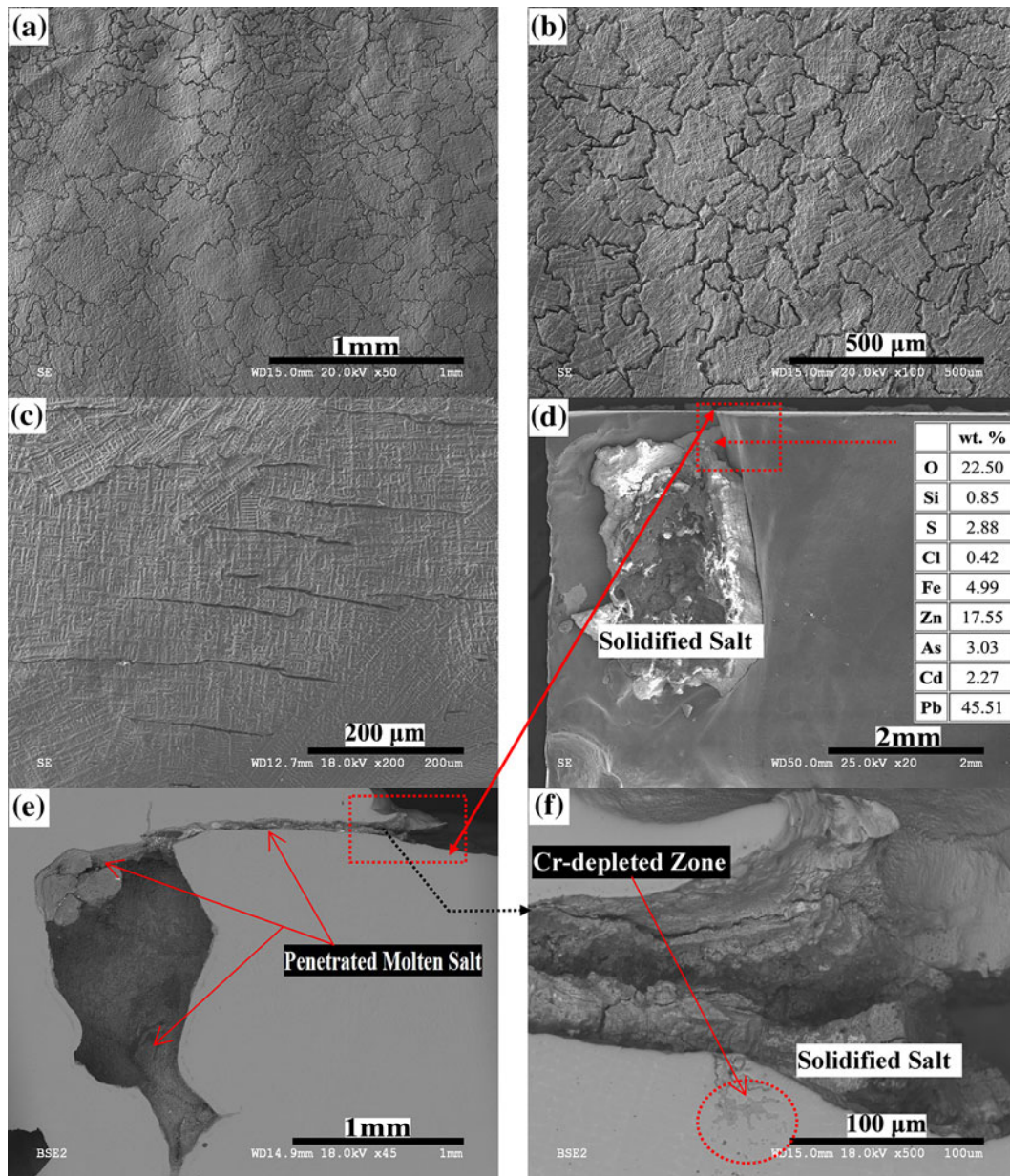
Fig. 12—[(*a*) to (*c*)] A network of well-developed circumferential cracks across the HSS of the weld overlay; (*d*) external view of a single well-developed, straight, and unbranched circumferential crack, which was located adjacent to the membrane and covered by the deposited salts and EDX elemental analysis of the deposits; and (*e*, *f*) cross-sectional view of the crack in (d), which shows the penetration of the molten phase into the weld layer through the crack, and subsequent degradation and Cr depletion in the weldment.

external (Figure 12(d)) and cross-sectional (Figures 12(e) and (f)) views. The EDX elemental analysis of the solidified salt that covered the crack is presented in Figure 12(d). The deposited salt was rich in Pb, Zn, and O. The depth of the crack and the initiation of the crack from the interface of the two weld beads as well as the penetration of the molten salt into the crack are apparent in the cross-sectional view of the crack in Figures 12(e) and (f). It should be noted that Figure 12(e) is part of Figure 8(f), which is shown again for clarifying the penetration depth of the molten salt into the cracks and the size of the crack. Obviously, this well-developed crack was deep enough to be connected to the

porosities inside the weld overlay, facilitating the penetration of the molten phase and corrosive species inside the weld layer. This is an obvious example to show how a combination of defects such as cracks and porosities as well as molten salt penetration can lead to the degradation/failure of the weld overlay. These findings indicated that the viscosity of the molten phase had been low enough to easily penetrate inside the deep cracks, as observed in Figures 12(d) through (f).

A Cr-depleted zone in the weld layer can be seen in Figure 12(f). More details of this Cr-depleted zone are shown in Figure 13(c) at a higher magnification. The chemical analysis of the penetrated molten salt and the
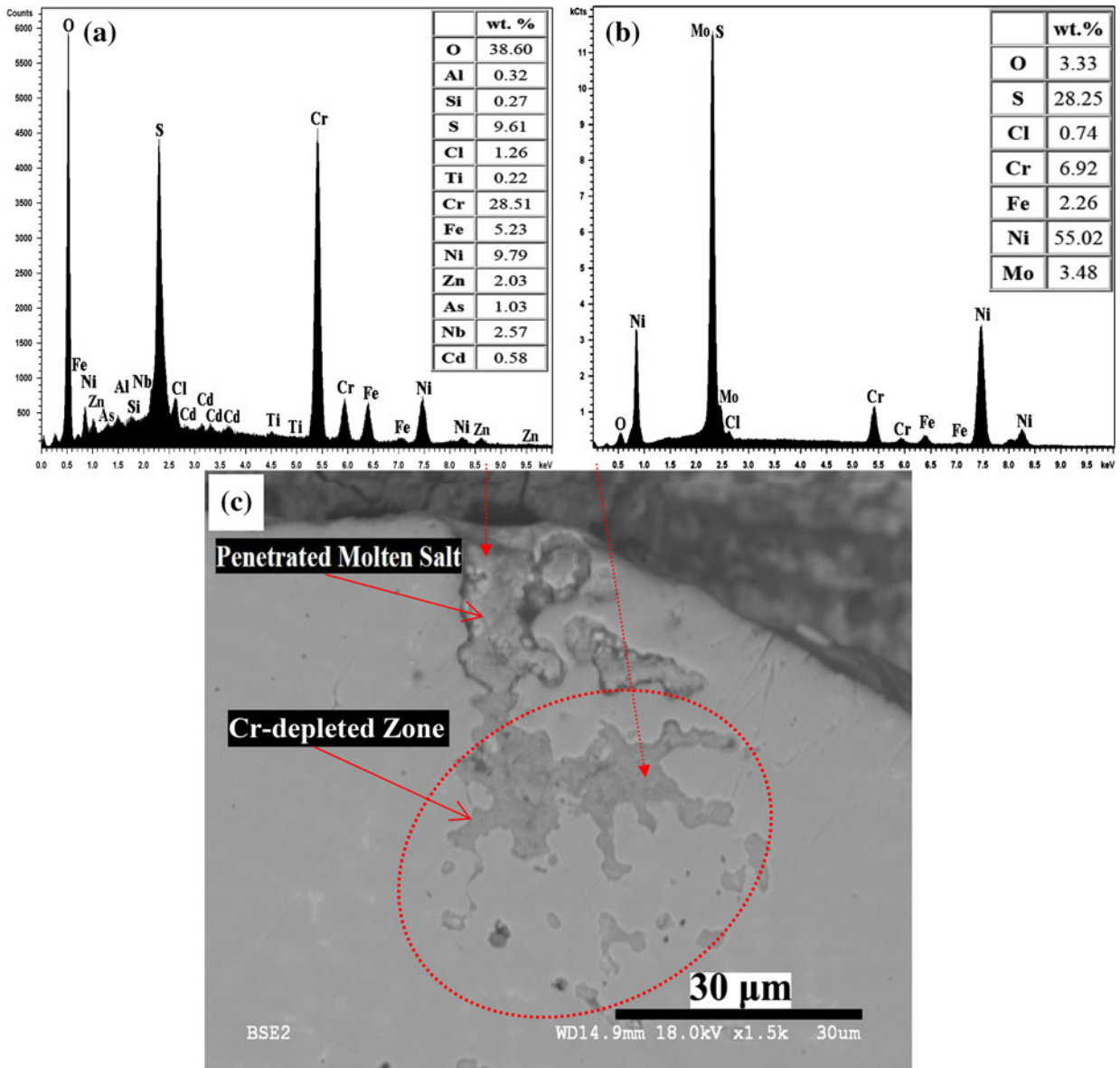
Fig. 13—EDX elemental analysis of locally penetrated molten phase into a region close to the Cr-depleted zone (*a*), and Cr-depleted zone (*b*); (*c*) cross-sectional SEM photomicrograph showing occurrence of Cr depletion in the weldment, exposed to the penetrated molten phase.

Cr-depleted zone is presented in Figures 13(a) and (b), respectively. Based on the EDX spectrum in Figure 13(a), dissolution of the alloying elements (Cr, Ni, Nb, Ti, and Fe) of the weld overlay alloy 625 into the penetrated molten phase was evident. Compared to the other alloy elements, particularly Ni, a high percentage of Cr in the penetrated molten phase (28.51 wt pct Cr *vs* 9.79 wt pct Ni) confirmed the highest tendency of Cr for dissolution when the weld overlay was exposed to the molten phase. The concentration of Cr in the Cr-depleted zone (6.92 wt pct) in the EDX spectrum of Figure 13(b), compared to the Cr concentration in the weld overlay (17.02 wt pct Cr, see Table I), is more evidence to confirm the strong tendency of Cr for dissolution in the molten phase. Selective oxidation of Cr can be mentioned as the main mechanism for the dissolution of Cr in the molten phase due to the presence of 38.60 wt pct

O in the EDX spectrum of Figure 13(a). This is in agreement with the findings of our previous reports.[1,10] Nb was not detected in the Cr-depleted zone because it fully dissolved and diffused into the molten phase, as can be observed in the EDX spectrum of Figure 13(a). Mo in the weld overlay was also prone to dissolution because its concentration in the Cr-depleted zone (3.48 wt pct) is less than the concentration of Mo in the weld overlay (6.00 wt pct, see Table I). Based on the EDX results, the Cr-depleted zone was enriched with S; accordingly, internal sulfidation was the mode of corrosion attack in the weld overlay alloy 625. The presence of 3.33 wt pct O in the EDX analysis of the Cr-depleted zone showed that internal oxidation can act as another mode of corrosion attack. In the presence of the molten phase, oxidation and sulfidation of the alloy accelerate after the depletion of Cr during the initiation
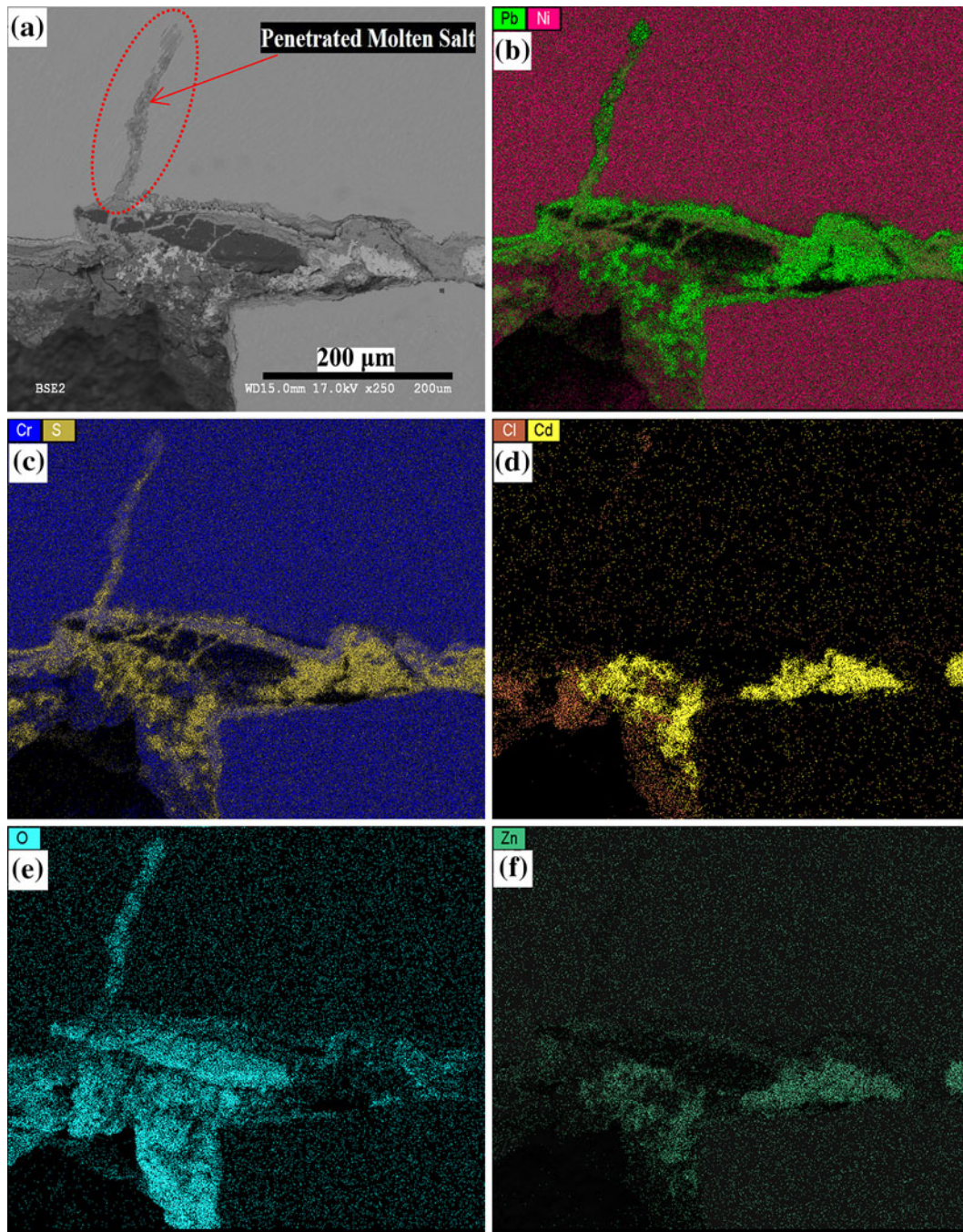
Fig. 14—X-ray mapping and spatial distribution of Pb, Zn, Cd, Ni, Cr, Cl, S, and O in the penetrated molten phase into the weld layer through a deep crack.

stage of hot corrosion attack.[1,45,46] Local penetration of the molten salt into the sites with low oxygen activity and Cr depletion in the weld alloy during the initiation stage of hot corrosion can easily occur when no external oxide forms on the surface. These factors are the main parameters to facilitate a rapid hot corrosion attack and ultimate failure of the weld layer at the propagation stage of hot corrosion, known also as the second stage of hot corrosion.[1]

X-ray mapping and spatial distribution of Pb, Zn, Cd, Ni, Cr, Cl, S, and O in the penetrated molten phase into

the weld layer through a deep crack can be seen in Figure 14. At the root of the crack, a well-developed channel provided a pathway for further penetration of the molten phase into the weld layer (Figure 14(a)). Penetration of the aggressive species (O, S, and Cl) into the channel was obvious in the relevant X-ray maps. The formation of such a kind of channel is a direct consequence of the molten phase penetration into the weld layer through open cracks and defects, accelerating the degradation and failure of the weld layer. Based on the X-ray mapping of S, Pb, Zn, and Cd, the penetrated

Penetrated Molten Phase	wt. %
O	5.09
S	26.84
Cl	0.26
Ni	1.15
Zn	14.00
As	1.48
Mo	0.37
Cd	50.82

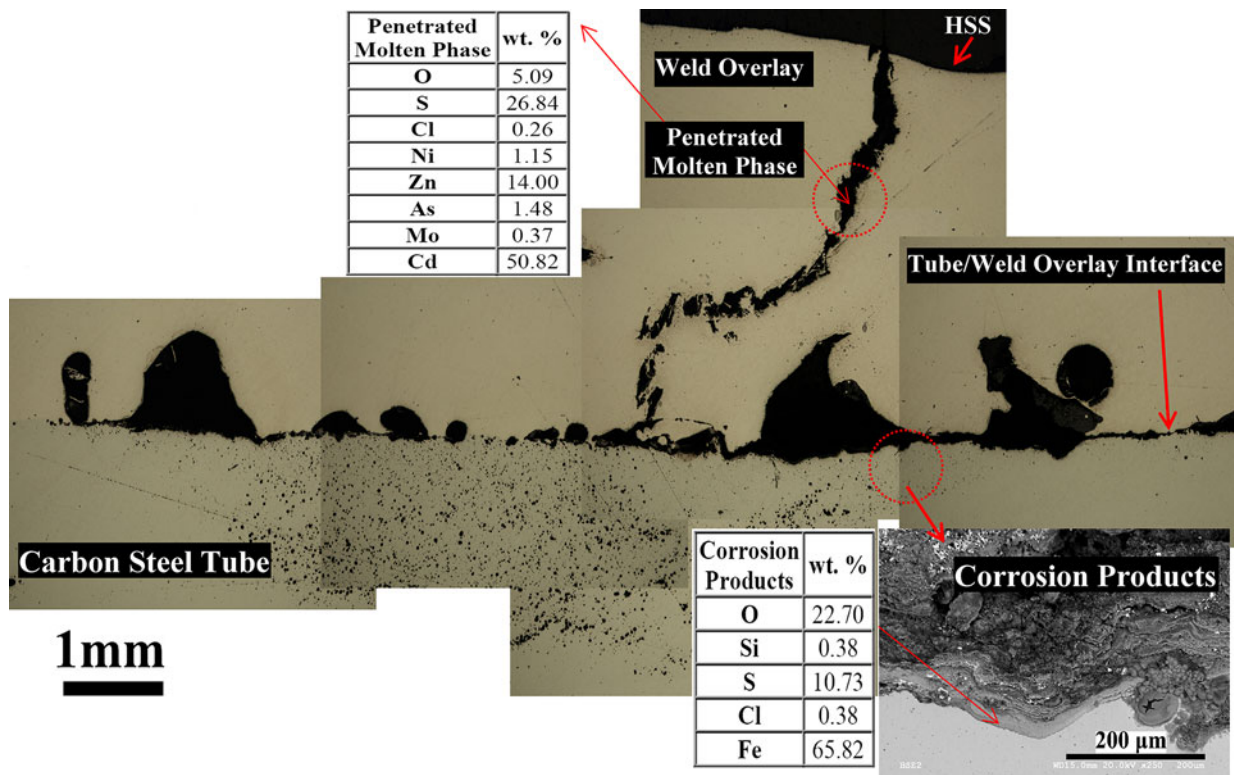| Corrosion Products	wt. %
O	22.70
Si	0.38
S	10.73
Cl	0.38
Fe	65.82

Fig. 15—Optical photomicrographs, presenting an open crack to the HSS which propagated through the entire weld overlay thickness, and EDX elemental analysis of the penetrated molten salt into the crack and corrosion products of the carbon steel tube.

S-rich phase is also rich in Pb, Zn, and Cd. X-ray mapping of Ni and Cr illustrated the dissolution of these two key alloying elements of the weld layer in the penetrated molten phase through sulfidation, oxidation, and chlorination mechanisms.

In Figure 15, an open crack to the HSS is shown. This crack propagated through the entire weld overlay thickness, and it is the most alarming type of crack. The presence of such cracks can preclude the use of alloy 625 as a weld overlay for protecting carbon steel tubes. This type of crack can lead to pitting corrosion and ultimate failure of the carbon steel tube, which allows water to leak onto the smelt bed. In such a case, there is a serious possibility for occurrence of a smelt/water explosion. Unfortunately, detecting such a type of crack is not always possible during a regular boiler inspection. The observed crack was straight and unbranched at the beginning, but after penetration some distance into the weld layer, signs of branching appeared. The occurred changes in the crack growth direction caused stepped crack morphology. This deep crack acted as a suitable pathway for the molten phase and the aggressive species to penetrate inside the weld overlay, reach the underlying substrate, and ultimately spread along the weld layer/tube interface. This caused further degradation of the tube and the weld layer. The crack was widened due to the action of the penetrated molten phase. EDX elemental analysis confirmed the presence of the penetrated molten salt inside the crack and in the locations close to the weld layer/substrate interface. A relatively poor correlation was observed between the analyses of the deposited salt mixture (Table IV) and the penetrated molten salt inside the cracks because of the inhomogeneous nature and layered structure of the deposited salts. When the crack reached the interface, because of the occurrence of hot corrosion attack along the weld layer/carbon steel tube interface, both weld layer and carbon steel tube significantly corroded and a large quantity of corrosion products accumulated in this region, as can be seen in the presented SEM image in Figure 15. Pitting corrosion in the carbon steel tube was a direct consequence of the molten salt penetration into the interface and hot corrosion attack. Oxidation and sulfidation of Fe were the main mechanisms of the carbon steel tube corrosion, as confirmed by EDX elemental analysis of the resultant corrosion products in Figure 15. The irregular shape and width of this crack and thorough SEM/EDX analysis of the crack pathway indicated that the growth of this crack gradually occurred due to the penetration of the molten phase into a circumferential crack or a surface defect in the early stage of degradation of the weld overlay.

Details of the propagation path of a branched crack, traversed through the entire thickness of the weld layer and intersected the weld layer/carbon steel interface, are presented in Figures 16(a) through (c). Accumulation of a significant amount of (Fe, O, S)-rich corrosion products at the interface of the weld layer/carbon steel tube indicated that more severe damage was caused by this type of crack propagated through the entire
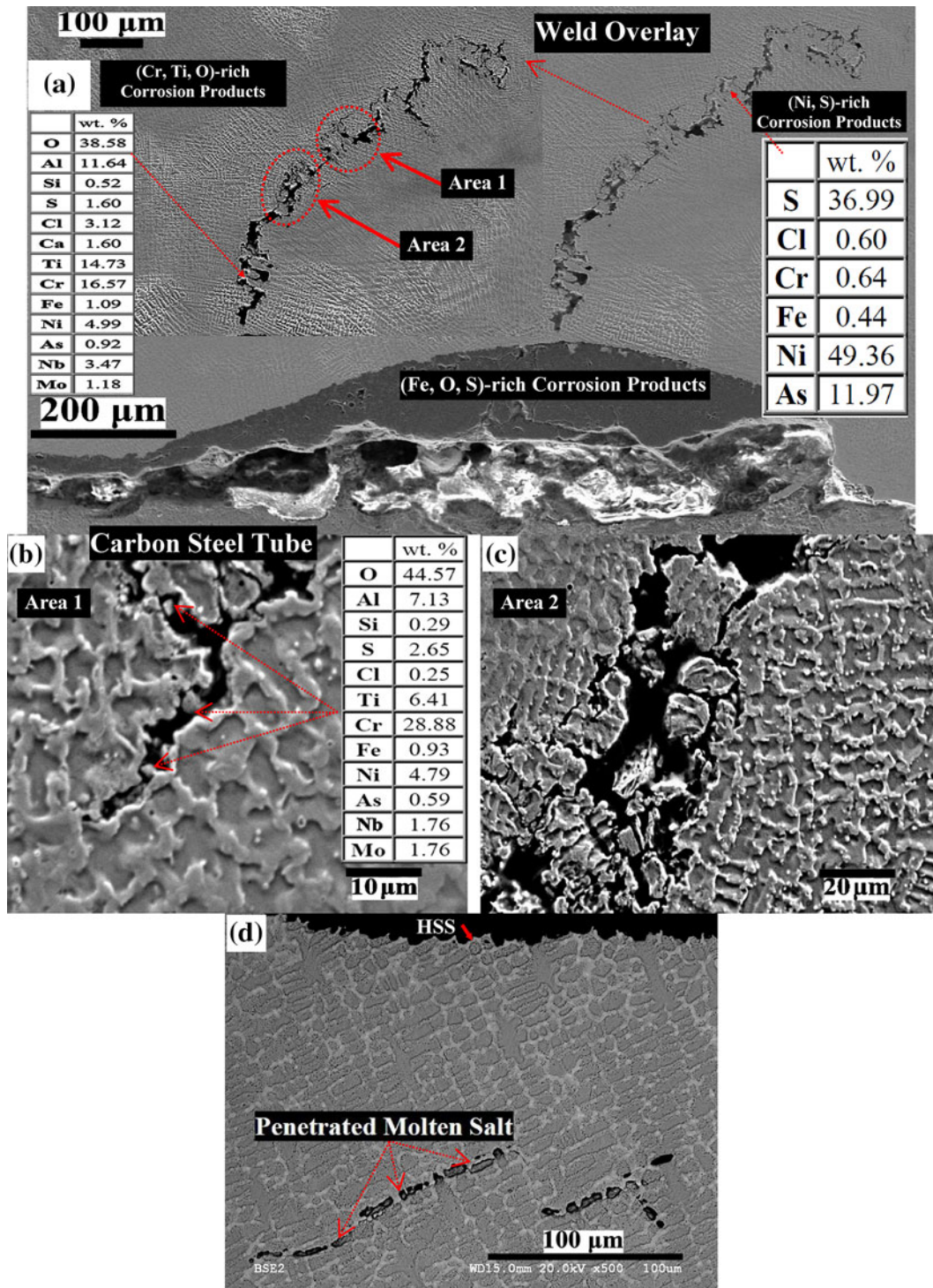
Fig. 16—Cross-sectional SEM photomicrographs of the weld overlay, showing propagation paths of a branched crack, which traversed through the entire thickness of the weld layer and intersected the weld layer/carbon steel interface as well as EDX elemental analysis of the corrosion products.

thickness of the weld layer. Many branched cracks, similar to those reported in Figures 15 and 16, are observed during the cross-sectional SEM study of the failed water wall. The branches were usually finer than the original crack. In some areas, signs of further branching observed in the cracks and a multi-branched morphology, also called the "river-delta pattern,"[47], were exhibited. Based on the EDX elemental analysis of the (Cr, Ti, O)-rich corrosion products in Figure 16(a), internal oxidation was the predominant mechanism for the dissolution of Cr and Ti alloying elements of the weld overlay alloy 625. Dissolution of Ni through
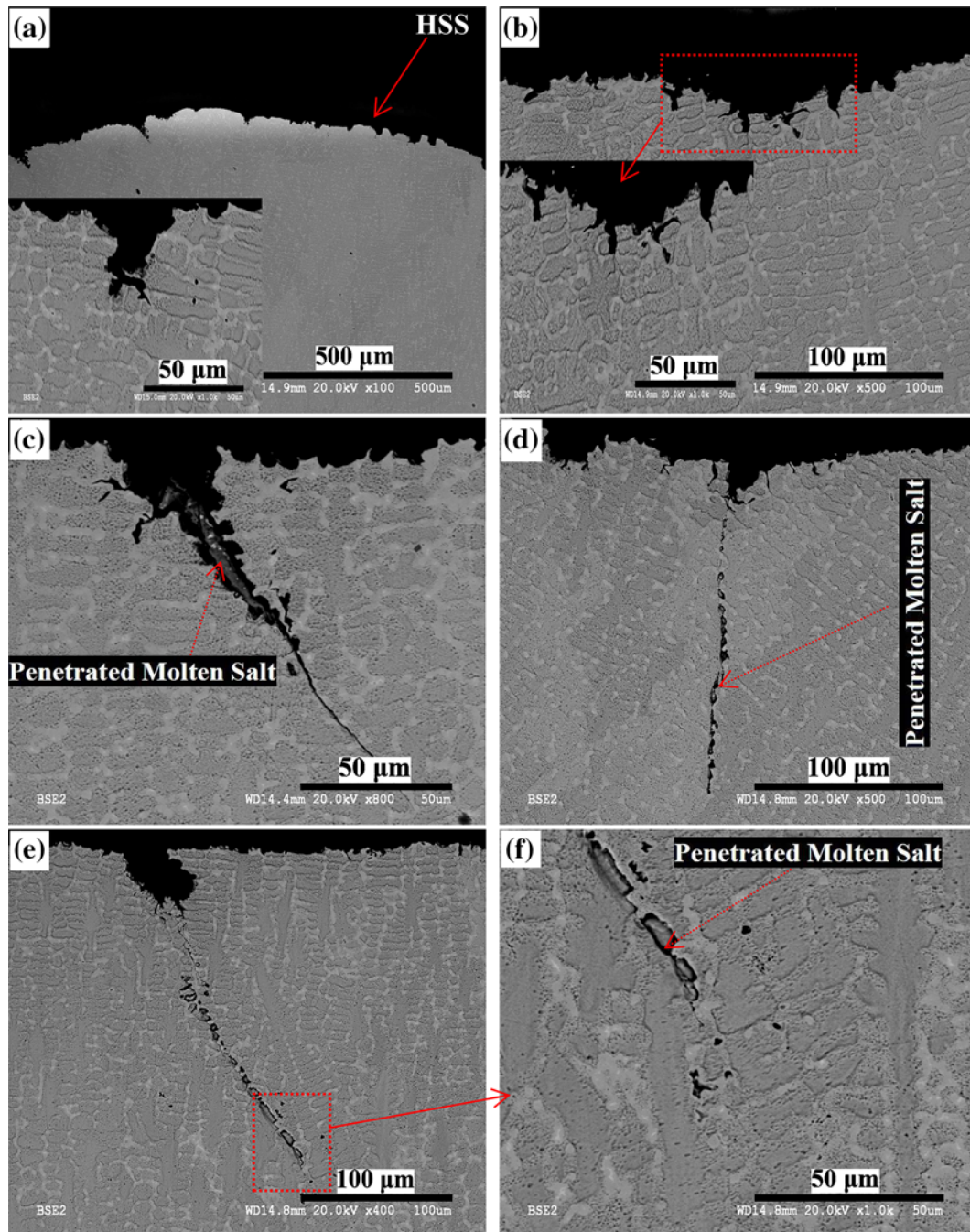
Fig. 17—Cross-sectional SEM photomicrographs of the weld overlay surface layer showing roughening of the HSS due to the occurrence of non-uniform preferential corrosion on the HSS (*a*, *b*), and the initiation of the cracks from the HSS [(*a*) to (*d*)], and the molten salt penetration into the initiated cracks along the dendrite cores (*e*, *f*).

internal sulfidation mechanism was confirmed because of the presence of 49.36 wt pct Ni and 36.99 wt pct S in the EDX elemental analysis of (Ni, S)-rich corrosion products in Figure 16(a). According to Figures 16(b) through (d), the dendrite cores are the preferential pathways for penetration of the molten salts and the crack branching. As was discussed before, the dendrite cores were depleted in Mo and Nb, but enriched with Fe, and appeared as a consequence of mixing of the weld overlay alloy 625 and the base metal/carbon steel. For these reasons, the dendrite cores acted as preferential

pathways for the molten salt penetration, which consequently facilitated crack growth and crack branching. This is in agreement with the findings of other studies which reported that corrosion occurs preliminary in the dendrite cores rather than the interdendritic regions.[27,48,49] In Figure 16(b), a high concentration of O and S in the dendrite cores, compared to the interdendritic regions, indicated the tendency of aggressive species (O and S) to diffuse inward mainly through the dendrite cores in the weld overlay, which caused the occurrence of internal oxidation and sulfidation.

Internal oxidation plays a detrimental role in a significant percentage of high temperature corrosion failure cases and it is known as a very destructive process in industrial applications.[50] Embrittlement and dilation of the alloy subsurface region might occur due to the presence of internally precipitated reaction products, which can cause the affected zone to flake off.[1] Internal oxidation and sulfidation are rapid because both phenomena are supported by diffusion of interstitial species (dissolved O and S) into the alloy dendritic microstructure.[1,50] In our previous reports,[1,10] internal sulfidation was also identified as a destructive mode of corrosion attack in hot corrosion failure of the wrought alloy 625 in a corrosive molten salt environment containing lead, zinc, iron, as well as sulfur, oxygen, and chlorine at 873 K, 973 K, and 1073 K (600 °C, 700 °C, and 800 °C), and grain boundaries were the preferential pathways for diffusion of O and S into the alloy during the occurrence of the hot corrosion phenomenon.

As can be seen in Figures 16(d) and 17, the non-uniform nature of the corrosion on the HSS of the water wall caused the roughening of the weld overlay surface. Microsegregation of alloying elements in the dendritic structure of the weld layer, discussed in Section III–B, was the main reason for the occurrence of the preferential corrosion on the HSS and the consequent roughening of the weld layer. Preferentially corroded zones can act as crack initiation sites, as observed in Figures 17(a) and (b). The conducted cross-sectional SEM studies on the HSS confirmed that cracks mainly initiated from the preferentially corroded and (Mo, Nb)-depleted dendritic cores on the HSS. The presence of the molten phase inside the developed surface cracks indicated that the penetration of the molten phase into the initiated surface cracks accelerated the propagation of the cracks mainly through the dendrite cores and further crack branching or caused the cracks to be widened. The outcome of this phenomenon was the development of some cracks like those reported in Figures 15 and 16. Initiation of the cracks from the dendrite cores of alloy 625 weld cladding was also reported by Luer et al.[40] As was extensively discussed in Section III–B, the weld layer was highly susceptible to solidification cracking along the Laves phase, (Mo, Nb)-rich regions. Solidification cracks, which are open to the surface, can also act as potential sites for penetration of the molten phase into the weld layer and gradual development of the cracks which intersect the weld layer/tube interface. An important point in Figure 17(d) is the formation of pores in the (Mo, Nb)-rich interdendritic regions, adjacent to the crack tip. Some pores were still at their early stage of development. Formation of pores in interdendritic regions, as a sign of internal hot corrosion attack, was a consequence of the aggressive species' (O and S) diffusion into the interdendritic regions, as was proved in our previous study.[1]

D. Hot Corrosion Study and Weight-Loss Measurement

Figure 18 shows the OCP curves of the weld overlay alloy 625 WEs at 873 K, 973 K, and 1073 K (600 °C, 700 °C, and 800 °C). Despite the potential fluctuations,

the OCP curves demonstrated an overall upward trend at the beginning of the exposure to the molten salt medium. Ultimately, the OCP of the WE reached a stable value after almost 24 hours. The OCP of the weld overlay alloy 625 WE was equal to 16, 15, and 14 mV at 873 K, 973 K, and 1073 K (600 °C, 700 °C and 800 °C), respectively. Rapid increase in the OCP of the WE upon exposure to the molten salt was attributed to the spontaneous growth of an anodic film on the surfaces of the electrode.[1] Extreme potential fluctuation in the OCP curve of the weld overlay at 1073 K (800 °C), even after 23 hours of exposure time, was evidence of unstable nature of the formed anodic film on the surface of the WE. The OCP curves at 873 K and 973 K (600 °C and 700 °C) reached a reasonably stable value after almost 8 hours of exposure; this means that a reasonably stable anodic film was formed on the surface of the WE at these two temperatures.

Potentiodynamic polarization curves of the weld overlay alloy 625 at 873 K, 973 K, and 1073 K (600 °C, 700 °C, and 800 °C), after 24 hours of exposure to the molten salt when the OCP curve reached a steady-state potential, are presented in Figure 19. In Figure 19, it is observed that anodic current density increased rapidly when the potential shifted in the noble direction; consequently, the weld overlay alloy 625 exhibited an active dissolution behavior at 873 K, 973 K, and 1073 K (600 °C, 700 °C, and 800 °C) and passivation of the alloy did not occur. This confirmed that the anodic film, which formed on the surface of the alloy, was a corrosion product layer, not an effective protective film/passive layer. The shape of the curves in Figure 19 is similar to those reported in our previous report for wrought alloy 625.[1] Corrosion potential (E_{corr}) determined from the potentiodynamic polarization curves and the calculated corrosion rate through the weight-loss measurement technique are presented in Table VI. As can be noted, the corrosion rate of the weld overlay in the molten salt medium increased by increasing the temperature due to a rise in the mobility of the electroactive species and ions as well as an increase in the mass fraction of the molten phase.[1]
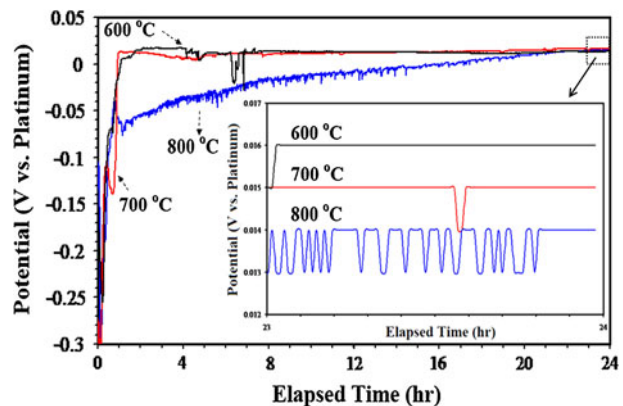

Fig. 18—OCP curves of the weld overlay alloy 625 electrodes, exposed to the molten salt mixture.

In Figure 20, SEM photomicrographs show the morphology of the attacked surface of the weld overlay alloy 625, after 24 hours of exposure to the molten salt mixture at 873 K, 973 K, and 1073 K (600 °C, 700 °C, and 800 °C). In addition to the general surface corrosion at all the investigated temperatures, the weld overlay was susceptible to the localized corrosion attack at 973 K and 1073 K (700 °C and 800 °C). This is why a network of pores formed on the attacked surface at these two temperatures, as can be seen in Figures 20(a) through (d). The susceptibility of the weld overlay to the pores' formation and pitting corrosion can justify the presence of many cavities on the surface of the weld layer, as observed in Figure 8. At 873 K (600 °C), the signs of general surface corrosion (Figure 20(e)) and preferential corrosion along the dendrite cores (Figure 20(f)) were observed on the attacked surface of the weld overlay. High percentage of Fe and depletion of Mo and Nb in the dendrite cores (based on Table V) made these regions susceptible to preferential corrosion attack, as was also mentioned before when the results in Figure 16 were discussed. Figure 21 shows cross-sectional SEM photomicrographs of the weld overlay alloy 625 corroded specimen at 873 K (600 °C). Penetration of the molten phase and the aggressive species through the developed channels/cracks and pathways across the subsurface regions of the overlay was evident. Oxidation of Fe in an Fe-rich inclusion, located in the subsurface regions of the overlay, was also noticeable in this image. Making a comparison between Figures 21 and 9(e) and (f) confirmed that the presence of Fe-rich inclusions in the weld overlay due to the dilution of Fe reduced the resistance of the weld overlay to the hot corrosion attack.
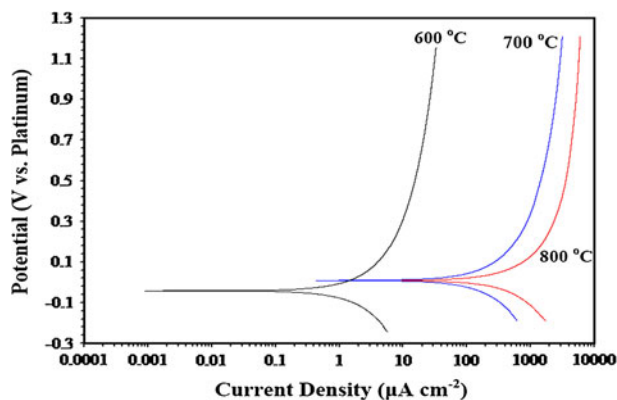

Fig. 19—Potentiodynamic polarization curves of the weld overlay alloy 625, exposed to the molten salt mixture at 873 K, 973 K, and 1073 K (600 °C, 700 °C, and 800 °C) for 24 h.

Chemical composition of the attacked surface of the weld overlay was determined by EDX elemental analysis, and the results are presented in Table VII. Compared to the chemical composition of the weld overlay alloy 625 in Table I (prior to high temperature electrochemical tests), the attacked surface of the weld overlay was depleted in Cr and Nb. This result was in agreement with the formation of Cr- and Nb-depleted zones in weld overlay, as observed in Figure 13. In the Cr-depleted surface at 973 K and 1073 K (700 °C and 800 °C), the concentration of Cr decreased to 6.30 and 1.94 wt pct, respectively, which were significantly lower than the concentration of Cr in the weld overlay in Table I (Cr: 17.02 wt pct). However, after 24 hours of exposure to the molten salt at 873 K (600 °C), the concentration of Cr (17.31 wt pct) was very close to the original composition of the weld overlay (17.02 wt pct). Based on this evidence, chromium is very prone to dissolution in molten salt during the exposure of the weld overlay alloy 625 to the molten salt at 973 and 1073 K (700 °C and 800 °C). Dissolution of Cr occurs during the initiation stage of hot corrosion.[1] Despite the fact that Cr is known as the most important alloying element in protecting wrought alloy 625 against corrosive environments at ambient temperature through the formation of the protective chromium-nickel oxide,[1] this element cannot play an effective role in providing protection for the weld overlay alloy 625 in the molten salt medium at the high temperature working conditions of the boiler. This is why the corrosion rate of the weld overlay in molten salt medium of the present study at 873 K, 973 K, and 1073 K (600 °C, 700 °C and 800 °C) was too high. At all the investigated temperatures, the concentration of Fe was significantly lower than the original concentration of Fe in the weld overlay alloy 625 (23.64 wt pct, reported in Table I). This showed that Fe content of the weld overlay was almost fully dissolved in the molten salt, confirming low resistance of the Fe element to the hot corrosion attack. Therefore, the presence of Fe in the weld overlay alloy 625, mainly through the carbon steel dilution during welding, reduced the overall resistance of the weld overlay to the hot corrosion attack in the molten salt medium.

The attacked surface of the weld overlay was rich in Ni and Mo at all the investigated temperatures. The concentrations of Ni and Mo in the weld overlay prior to the exposure to the molten salt were around 47.46 and 6.00 wt pct, respectively. The concentration of (Ni, Mo) in the surface layer increased to (61.79, 9.73), (70.26, 14.17), and (70.32, 11.2) wt pct after 24 hours of exposure to the molten salt at 873 K, 973 K, and 1073 K (600 °C, 700 °C and 800 °C), respectively, which was considerably higher than the concentration of

Table VI. Obtained Corrosion Potential from the Potentiodynamic Polarization Curves and the Calculated Corrosion Rate Through Weight-Loss Measurement Technique for Weld Overlay Alloy 625, Exposed to the Molten Salt Mixture at 873 K, 973 K, and 1073 K (600 °C, 700 °C, and 800 °C) for 24 h

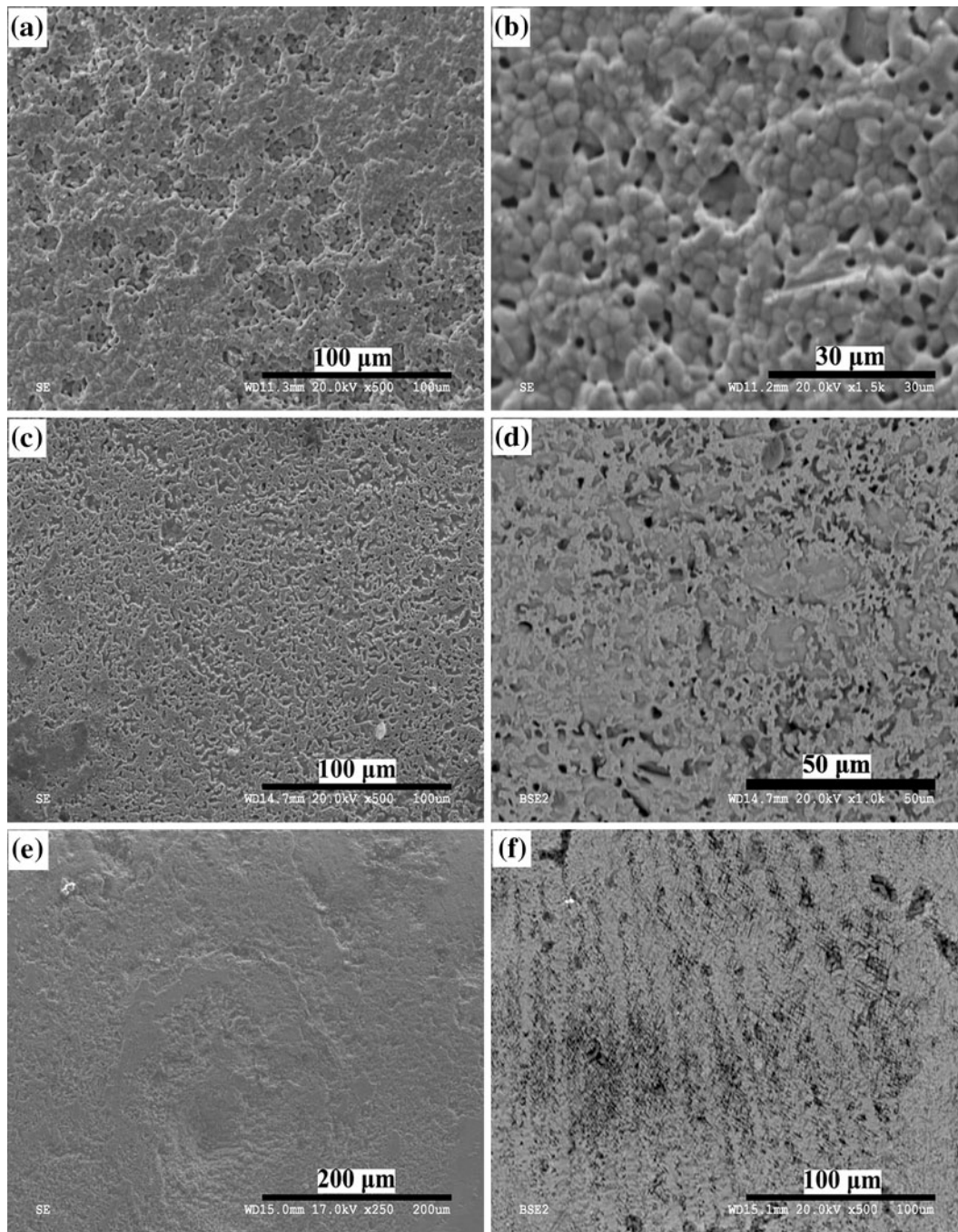|	1073 K (800 °C)	973 K (700 °C)	873 K (600 °C)
E_{corr} (mV vs Platinum)	9.0	9.5	−41.5
Corr. Rate (mm/Year)	22.75	17.03	1.69

Fig. 20—SEM photomicrographs of the surfaces of the weld overlay alloy 625 corroded specimens at 1073 K (800 °C) (*a*, *b*), 973 K (700 °C) (*c*, *d*), and 873 K (600 °C) (*e*, *f*), which show the morphology of the attacked surfaces after cleaning and removing the corrosion products and the scales according to ASTM G1-03.

Ni and Mo in the weld overlay prior to the exposure. Considering the depletion of Cr in the surface layer of the attacked weld overlay and high concentration of Ni and Mo in this layer, it can be concluded that after 24 hours of exposure to the molten salt, a (Ni, Mo)-rich layer formed on the surface. This layer was also rich in oxygen, particularly at 1073 K (800 °C) as reported in Table VII. However, this (Ni, Mo, O)-rich layer was highly porous and was not able to act as an effective barrier layer to protect the weld overlay against the hot corrosion attack, which can be supported by the high corrosion rate of the weld overlay, determined through weight-loss measurement technique and tabulated in Table VI, and SEM results in Figures 20 and 21.

The concentration of the dissolved Mo in the molten salt mixture, measured by means of the ICP/AAS technique, was less than 1 ppm (lower than the detection limit of ICP/AAS) at all the investigated temperatures.
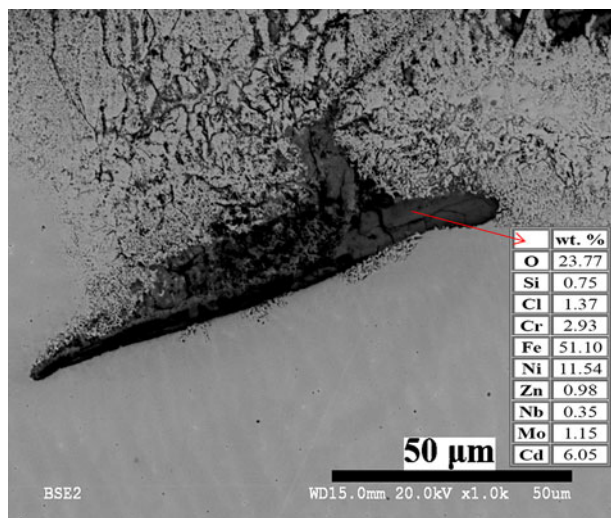
	wt. %
O	23.77
Si	0.75
Cl	1.37
Cr	2.93
Fe	51.10
Ni	11.54
Zn	0.98
Nb	0.35
Mo	1.15
Cd	6.05

Fig. 21—Cross-sectional SEM photomicrographs of the weld overlay alloy 625 corroded specimen at 873 K (600° C), which show the penetration of molten phase to the subsurface region of the weld layer through the developed channels and cracks and oxidation of an Fe-rich inclusion, located close to the surface layer.

Table VII. EDX Elemental Analysis (Weight Percent) from the Attacked Surface of the Weld Overlay Alloy 625 Corroded Samples Exposed to the Molten Salt Mixture at 873 K, 973 K, and 1073 K (600 °C, 700 °C, and 800 °C) for 24 h

	Attacked Surface of Weld Overlay Alloy 625		
	1073 K (800 °C)	973 K (700 °C)	873 K (600 °C)
Ni	70.32 ± 3.06	70.26 ± 2.16	61.79 ± 4.06
Cr	1.94 ± 0.31	6.30 ± 1.90	17.31 ± 2.01
Mo	11.20 ± 0.92	14.17 ± 1.93	9.73 ± 1.61
Nb	0.71 ± 0.96	1.26 ± 0.27	1.97 ± 0.41
Ti	0	0	0.24 ± 0.14
O	14.00 ± 1.81	6.64 ± 1.32	3.71 ± 2.64
Fe	1.32 ± 0.16	0	0.63 ± 0.17
Al	0.18 ± 0.10	0.44 ± 0.17	0.18 ± 0.10
Si	0.12 ± 0.08	0.52 ± 0.20	0.14 ± 0.09
Cl	0.17 ± 0.07	0.41 ± 0.20	2.63 ± 2.51

The amounts of the dissolved chromium and nickel in the molten salt mixture were determined as Ni, 34, 28, and 31 ppm at 1073 K, 973 K, and 873 K (800 °C, 700 °C, and 600 °C), respectively, and Cr, 61, 37, and 15 at 1073 K, 973 K, and 873 K (800 °C, 700 °C, and 600 °C), respectively.

IV. CONCLUSIONS

The deposited salt mixtures on the water wall had a strong tendency to form a molten phase at the operating temperature range of the radiant boiler as confirmed by DTA results. The presence of the deposited salt mixtures and the formation of the molten phase led to the occurrence of the hot corrosion attack in the water wall and the ultimate failure of the weld overlay. The coating, which was performed as a weld overlay and also remelted with GTAW process, was not able to protect boiler tubes from the smelter environment. Weld overlay alloy 625 exhibited a well-defined anisotropic, dendritic structure. A bright/white structure in the interdendritic regions pertained to the Laves phase. The white areas (Laves) were rich in Mo and Nb. Based on the EDX results, the dendrite cores were depleted in Nb and Mo, while they contained higher concentration of Fe, Ni, and Cr, compared to the interdendritic regions. Solidification cracks were found to be associated with the interdendritic regions due to the presence of the Laves constituent.

The high heat input caused an increase in the dilution level of Fe because the carbon steel substrate melted in the weld pool temperature. The dilution level was determined based on the concentration of Fe in the weld overlay, the filler metal, and the carbon steel tube (base metal). The dilution and consequently the presence of a significant amount of Fe in the weldment composition were the key issues in the alloy 625 weld overlay. The high heat input and the dilution were also reasons for the formation of Fe-rich inclusions in the welding structure. As confirmed by the laboratory-scale hot corrosion study, the Fe-rich inclusions were susceptible to the hot corrosion attack, when the weld overlay was exposed to the corrosive environment of the boiler. Consequently, these inclusions reduced the resistance of the weld overlay alloy 625 to the molten salt-induced corrosion.

SEM analysis confirmed the presence of a network of well-developed circumferential cracks across the surface of the weld overlay. SEM/EDX results together with the laboratory-scale hot corrosion study indicated that a combination of defects, such as cracks and porosities, and the molten salt penetration into the weld overlay through the cracks/defects led to the degradation and ultimate failure of the weld overlay. It was confirmed that Cr, Nb, and Fe elements in the chemical composition of the weld overlay alloy 625 have the highest tendency to be dissolved in the molten salt medium, compared to other alloying elements in weld alloy 625 (particularly Ni), when the weld overlay was exposed to the molten phase. This caused the formation of Cr- and Nb-depleted zones in the weld overlay. Internal sulfidation and oxidation were identified as two modes of hot corrosion attack in the weld overlay alloy 625.

The cracks, which initiated from the HSS and traversed through the entire thickness of the weld layer and ultimately intersected the weld layer/carbon steel interface, were the most alarming type of cracks. As confirmed by SEM and optical microscope results, these deep and branched cracks acted as suitable pathways for the molten phase to penetrate inside the weld overlay, reach the underlying substrate, and spread along the weld layer/tube interface. SEM/EDX results showed that the dendrite cores acted as the preferential pathways for the molten salt penetration and diffusion of the aggressive species (O, S). Consequently, the penetration of the molten phase into the cracks accelerated the propagation of the cracks and it facilitated further crack branching. Pitting corrosion in the carbon steel tube was a direct consequence of the molten salt penetration into the weld/tube interface and subsequent hot corrosion

attack. Oxidation and sulfidation of Fe were identified as the main mechanisms of the carbon steel tube hot corrosion. The cracks mainly initiated from the preferentially corroded and (Mo, Nb)-depleted dendritic cores on the HSS. The solidification cracks, which are open to the surface, can also act as potential sites for penetration of the molten phase into the weld layer and gradual development of the cracks which intersect the weld layer/tube interface.

The hot corrosion study confirmed that after 24 hours of exposure to the molten salt, a (Ni, Mo, O)-rich layer formed on the surface. However, this layer was not able to act as an effective barrier layer to protect the weld overlay against the hot corrosion attack because of the high corrosion rate of the specimens, determined through the weight-loss measurement technique and porous nature of this layer.

V. RECOMMENDATIONS

Considering the conducted studies on the failed weld overlay alloy 625 and the reviewed literature in the present manuscript, the following recommendations can be presented:

1. The content of Fe in the weld overlay alloy should be kept to less than 6 to 7 pct to minimize the adverse effects of Fe on the properties of the deposited weld layer. The dilution level of Fe can be controlled by controlling the heat input.
2. By decreasing the arc power/heat input and increasing the volumetric filler metal feed rate (deposition rate), which means maximizing filler metal feed rate-to-arc power ratio, the dilution level and Fe content in the overlay will be minimized. This can ultimately lead to improving the cracking and corrosion resistance of the weld overlay and avoid the formation of undesirable phases and inclusions such as Fe-rich inclusions.
3. It is recommended to use a pulsating direct current for applying weld overlay to control the segregation and dilution phenomena in the weldment and to reduce heat buildup, residual stress, and distortion during the welding process.
4. In addition to minimizing the heat input, a high weld metal cooling rate has to be used to decrease the Nb segregation and amount of detrimental Laves phase, thereby reducing the susceptibility to the occurrence of the solidification cracking. Circulating water inside the tubes during deposition of the weld layer is an effective option to increase the cooling rate of the weldment and to reduce the microsegregation and Laves formation when applying the weld overlay on the water walls.
5. Selecting a filler metal with relatively high content of C and low content of Si and Fe to promote the formation of γ/NbC at the terminal stage of the overlay solidification at the expense of the γ/Laves is another precaution for decreasing the solidification temperature range and, therefore, reducing the cracking susceptibility.
6. Compared to other alloying elements in alloy 625, Mo and Ni showed the highest resistance to hot corrosion and dissolution in the molten phase. It is recommended to look at the possibility of applying Inconel 622 or Inconel 686 due to (a) the presence of higher concentration of Mo in these two alloys and (b) replacement of Nb with W compared to Inconel 625. Further research on these two alloys and their hot corrosion properties is being conducted by the present authors.

REFERENCES

1. E. Mohammadi Zahrani and A.M. Alfantazi: *Corros. Sci.*, 2012, vol. 65, pp. 340–59.
2. Y.I. Sannikov, M.A. Liamina, V.A. Shumskij, and M.V. Radashin: *CIM Mag.*, 1998, vol. 91, pp. 76–81.
3. D.W. Goosen, and M.T. Martin: *Application of KIVCET Smelting Technology at Cominco, Mining Millennium Conference*, Toronto, ON, 2000, pp. 1–20.
4. G.Y. Lai and N. Blogg: *OMMI*, 2004, vol. 3, pp. 1–19.
5. Y. Kawahara: *J. Therm. Spray Technol.*, 2007, vol. 16, pp. 202–13.
6. J. Kalivodova, D. Baxter, M. Schutze, and V. Rohr: *Mater. Corros.*, 2008, vol. 59, pp. 367–73.
7. M.A. Uusitalo, P.M.J. Vuoristo, and T.A. Mantyla: *Corros. Sci.*, 2004, vol. 46, pp. 1311–31.
8. T.S. Sidhu, R.D. Agrawal, and S. Prakash: *Surf. Coat. Technol.*, 2005, vol. 198, pp. 441–46.
9. T.S. Sidhu, S. Prakash, and R.D. Agrawal: *Curr. Sci.*, 2006, vol. 90, pp. 41–47.
10. E. Mohammadi Zahrani and A. Alfantazi: *Metall. Mater. Trans. A*, 2012, vol. 43A, pp. 2857–68.
11. S. Lee, N.J. Themelis, and M.J. Castaldi: *J. Therm. Spray Technol.*, 2007, vol. 16, pp. 104–110.
12. H. Zwaher: *Ways to Improve the Efficiency of Waste to Energy Plants for the Production of Electricity and Reusable Materials, 11th North America WTE Conference*, Tampa, FL, 2003.
13. "Standard Guide for Preparation of Metallographic Specimens", American Society for Testing and Materials, ASTM E3-11, 2011, pp. 1–13.
14. "Corrosion of Metals and Alloys—Method for Metallographic Examination of Samples after Exposure to High-Temperature Corrosive Environments", International Organization for Standardization, ISO/DIS 26146.
15. J.R. Davis: *ASM Specialty Hand Book: Nickel, Cobalt and Their Alloys*, ASM International, Materials Park, OH, 2000, p. 301.
16. E. Mohammadi Zahrani, A. Alfantazi, and D. Verhelst: *ECS Trans.*, 2010, vol. 28, pp. 171–85.
17. "Standard Test Method for Conducting Potentiodynamic Polarization Resistance Measurements", American Society for Testing and Materials, ASTM G59-97, 2009, pp. 1–4.
18. "Standard Reference Test Method for Making Potentiostatic and Potentiodynamic Anodic Polarization Measurements", American Society for Testing and Materials, ASTM G5-94, 2004, pp. 1–12.

19. "Standard Practice for Preparing, Cleaning, and Evaluating Corrosion Test Specimens", American Society for Testing and Materials, ASTM G1-03, 2011, pp. 1–9.
20. J.N. Pires, A. Loureiro, and G. Bolmsjo: *Welding Robots: Technology, System Issues and Applications*, Springer, London, 2006.
21. J.N. Dupont, S.W. Banovic, and A.R. Marder: *Weld. J.*, 2003, vol. 82 (6), pp. 125s–135s.
22. S.W. Banovic, J.N. Dupont, and A.R. Marder: *Metall. Mater. Trans. B*, 2001, vol. 32B, pp. 1171–76.
23. M.J. Cieslak, T.J. Headley, T. Kollie, and A.D. Romig: *Metall. Trans. A*, 1988, vol. 19A, pp. 2319–31.
24. M.J. Cieslak: *Weld. J.*, 1991, vol. 70, pp. 49s–56s.
25. J.N. Dupont: *Metall. Mater. Trans. A*, 1996, vol. 27A, pp. 3612–20.
26. J.N. Dupont, C.V. Robino, J.R. Michael, M.R. Notis, and A.R. Marder: *Metall. Mater. Trans. A*, 1998, vol. 29A, pp. 2785–96.
27. K. Chandrasekaran, N.S. Tiedje, and J. Hald: *Int. J. Cast Met. Res.*, 2009, vol. 22, pp. 306–310.
28. J. Adamiec: *Mater. Charact.*, 2009, vol. 60, pp. 1093–99.
29. M.C. Maguire, and J.R. Michael: *Superalloys 718, 625, 706 and Various Derivatives*, E.A. Loria, ed., TMS, Pittsburgh, PA, 1994, pp. 881–92.
30. H. Hanninen, A. Brederholm, and T. Saukkonen: *Hot Cracking Phenomena in Welds II*, Springer, Berlin, 2008, pp. 171–91.
31. G. Lai: *1998 TAPPI Engineering & Papermaking Conference Proceedings*, TAPPI Press, Miami, FL, 1998, pp. 417–30.
32. J.R. Kieser, B. Taljat, X.-L. Wang, R. Swinderman, P. Maziasz, R. Thomas, E. Payzant, D. Singbeil, and R. Prescott: *1997 TAPPI Engineering & Papermaking Conference Proceedings*, TAPPI Press, Atlanta, GA, 1997, pp. 1025–41.
33. A. Philip and P.E. Schweitzer: *Fundamentals of Metallic Corrosion: Atmospheric and Media Corrosion of Metals*, CRC Press, New York, N.Y., 2007.
34. F. Wang and Y. Shu: *Oxid. Met.*, 2003, vol. 59, pp. 201–14.
35. H.J. Grabke, M. Spiegel, and A. Zhas: *Mater. Res.*, 2004, vol. 7, pp. 89–95.
36. C.H. Radhakrishna and K. Prasad Rao: *J. Mater. Sci.*, 1997, vol. 32, pp. 1977–84.
37. M.J. Cieslak, G.A. Knorovski, T.J. Headley, and A.D. Romig: *Metall. Mater. Trans. A*, 1986, vol. 17A, pp. 2107–16.
38. J.N. Dupont: *Weld. J.*, 1999, vol. 78 (7), pp. 253s–263s.
39. G.A. Knorovsky, M.J. Cieslak, T.J. Headley, A.D. Romig, and W.F. Hammetter: *Metall. Trans. A*, 1989, vol. 29A, pp. 2149–58.
40. K. Luer, J. Dupont, A. Marder, and C. Skelonis: *Mater. High Temp.*, 2001, vol. 18, pp. 11–19.
41. F. Cortial, J.M. Corrieu, and C. Vernot-loier: *Metall. Mater. Trans. A*, 1995, vol. 26A, pp. 1273–86.
42. J.N. Dupont and A.R. Marder: *Metall. Mater. Trans. B*, 1996, vol. 27B, pp. 481–89.
43. N. Karunakaran and V. Balasubramanian: *Trans. Nonferrous Met. Soc. China*, 2011, vol. 21, pp. 278–86.
44. J.J. Schirra, R.H. Caless, and R.W. Hatala: *Superalloys 718, 625 and Various Derivatives*, E.A. Loria, ed., TMS, Pittsburgh, PA, 1991, pp. 375–88.
45. P. Hancock: *Mater. Sci. Technol.*, 1987, vol. 3, pp. 536–44.
46. I.G. Wright: *Metals Handbook*, 9th ed., vol. 13, ASM, Materials Park, OH, 1987, pp. 97–103.
47. D. Singbeil, B. Prescott, J. Keiser, and B. Swindeman: *1997 TAPPI Engineering & Papermaking Conference Proceedings*, TAPPI Press, Nashville, TN, 1997, pp. 1001–24.
48. M. Montgomery, O. Biede, and O.H. Larson: *Mater. Sci. Forum*, 2006, vols. 522–523, pp. 523–30.
49. C. Hojerslev, N. Tiedje, and J. Hald: in *Proc. Danish Metallurgical Soc. Winter Meeting*, Kolding, Denmark, 2005.
50. R.C. John: in *NACE Corrosion Conference*, NACE International, Houston, TX, 1996, p. 171.